

# The EDGE-CALIFA Survey: Spatially Resolved $^{13}\text{CO}(1-0)$ Observations and Variations in $^{12}\text{CO}(1-0)/^{13}\text{CO}(1-0)$ in Nearby Galaxies on kpc Scales

YIXIAN CAO,<sup>1,2</sup> TONY WONG,<sup>1</sup> ALBERTO D. BOLATTO,<sup>3</sup> ADAM K. LEROY,<sup>4</sup> ERIK ROSOLOWSKY,<sup>5</sup> DYAS UTOMO,<sup>6</sup> SEBASTIÁN F. SÁNCHEZ,<sup>7</sup> JORGE K. BARRERA-BALLESTEROS,<sup>7</sup> REBECCA C. LEVY,<sup>8,\*</sup> DARIO COLOMBO,<sup>9</sup> LEO BLITZ,<sup>10</sup> STUART N. VOGEL,<sup>3</sup> JOHANNES PUSCHNIG,<sup>11</sup> VICENTE VILLANUEVA,<sup>3</sup> AND MONICA RUBIO<sup>12</sup>

<sup>1</sup>*Department of Astronomy, University of Illinois, Urbana, IL 61801, USA*

<sup>2</sup>*Max-Planck-Institut für extraterrestrische Physik, Giessenbachstraße 1, D-85748 Garching, Germany*

<sup>3</sup>*Department of Astronomy, University of Maryland, College Park, MD 20742, USA*

<sup>4</sup>*Department of Astronomy, The Ohio State University, 140 West 18th Avenue, Columbus, Ohio 43210, USA*

<sup>5</sup>*Department of Physics, University of Alberta, Edmonton, AB T6G 2E1, Canada*

<sup>6</sup>*National Radio Astronomy Observatory, 520 Edgemont Road, Charlottesville, VA 22903-2475, USA*

<sup>7</sup>*Instituto de Astronomía, Universidad Nacional Autónoma de México, A.P. 70-264, 04510 México, D.F., Mexico*

<sup>8</sup>*Steward Observatory, University of Arizona, Tucson, AZ 85721, USA*

<sup>9</sup>*Max-Planck-Institut für Radioastronomie, D-53121, Bonn, Germany*

<sup>10</sup>*Department of Astronomy, University of California, Berkeley, CA 94720, USA*

<sup>11</sup>*Universität Bonn, Argelander-Institut für Astronomie, Auf dem Hügel 71, D-53121 Bonn, Germany*

<sup>12</sup>*Departamento de Astronomía, Universidad de Chile, Casilla 36-D, Santiago, Chile*

## ABSTRACT

We present  $^{13}\text{CO}(J=1\rightarrow 0)$  observations for the EDGE-CALIFA survey, which is a mapping survey of 126 nearby galaxies at a typical spatial resolution of 1.5 kpc. Using detected  $^{12}\text{CO}$  emission as a prior, we detect  $^{13}\text{CO}$  in 41 galaxies via integrated line flux over the entire galaxy, and in 30 galaxies via integrated line intensity in resolved synthesized beams. Incorporating our CO observations and optical IFU spectroscopy, we perform a systematic comparison between the line ratio  $\mathcal{R}_{12/13} \equiv I[^{12}\text{CO}(J=1\rightarrow 0)]/I[^{13}\text{CO}(J=1\rightarrow 0)]$  and the properties of the stars and ionized gas. Higher  $\mathcal{R}_{12/13}$  values are found in interacting galaxies than in non-interacting galaxies. The global  $\mathcal{R}_{12/13}$  slightly increases with infrared color  $F_{60}/F_{100}$ , but appears insensitive to other host galaxy properties such as morphology, stellar mass, or galaxy size. We also present annulus-averaged  $\mathcal{R}_{12/13}$  profiles for our sample up to a galactocentric radius of  $0.4r_{25}$  ( $\sim 6$  kpc), taking into account the  $^{13}\text{CO}$  non-detections by spectral stacking. The radial profiles of  $\mathcal{R}_{12/13}$  are quite flat across our sample. Within galactocentric distances of  $0.2r_{25}$ , azimuthally-averaged  $\mathcal{R}_{12/13}$  increases with star formation rate. However, the Spearman rank correlation tests show the azimuthally-averaged  $\mathcal{R}_{12/13}$  does not strongly correlate with any other gas or stellar properties in general, especially beyond  $0.2r_{25}$  from the galaxy centers. Our findings suggest that in the complex environments in galaxy disks,  $\mathcal{R}_{12/13}$  is not a sensitive tracer for ISM properties. Dynamical disturbances, like galaxy interactions or the presence of a bar, also have an overall impact on  $\mathcal{R}_{12/13}$ , which further complicate the interpretations of  $\mathcal{R}_{12/13}$  variations.

*Keywords:* galaxies: ISM – galaxies: evolution – ISM: molecules

## 1. INTRODUCTION

The molecular interstellar medium (ISM) plays a critical role in galaxy evolution, serving as the fuel for star formation in galaxies. Large scale processes accumulate the gas and regulate the abundance and properties of molecular clouds. In turn, the gas properties on local cloud scales control the star formation process which drives the evolution of the entire galaxy. It is therefore

Corresponding author: Yixian Cao  
ycao@mpe.mpg.de

\* NSF Astronomy and Astrophysics Postdoctoral Fellow

important to understand how local and global properties of galaxies affect the molecular gas.

In nearby galaxies,  $^{12}\text{CO}(J = 1 \rightarrow 0)$  is the most commonly used tracer of molecular gas. However,  $^{12}\text{CO}(J = 1 \rightarrow 0)$  is typically optically thick, and its optical depth can vary. Because the isotopologue  $^{13}\text{CO}$  is much less abundant in galaxies (e.g. Wilson & Rood 1994; Henkel et al. 2014), its lines tend to be optically thin and offer a powerful complement to  $^{12}\text{CO}(J = 1 \rightarrow 0)$ . The line intensity ratio  $\mathcal{R}_{12/13} \equiv I[^{12}\text{CO}(J = 1 \rightarrow 0)]/I[^{13}\text{CO}(J = 1 \rightarrow 0)]$  can be used to trace variations in optical depth of molecular gas, with the caveat that  $\mathcal{R}_{12/13}$  can also be influenced by chemical processes.

Because the emission of  $^{13}\text{CO}$  is weaker and more difficult to observe, interferometric mapping studies of this line have been only made in a small number of galaxies, often focusing on a single target each time (e.g. Meier & Turner 2004; Rosolowsky & Blitz 2005; Aalto et al. 2010; Pety et al. 2013; Sliwa et al. 2017; Gallagher et al. 2018). Resolved  $\mathcal{R}_{12/13}$  values ranging from  $\sim 4$  to  $\sim 25$  have been reported in these studies. Previous single dish studies found that the galaxy-integrated  $\mathcal{R}_{12/13}$  correlates with *IRAS* IR color and the average star formation rate (SFR) surface density, indicating lower opacity in more active, hotter systems (Young & Sanders 1986a; Aalto et al. 1991; Sage & Isbell 1991; Davis 2014). In contrast to these galaxy-integrated studies, studies comparing resolved  $\mathcal{R}_{12/13}$  estimates to the SFR surface density within galaxies have not found a strong correlation (e.g. Cao et al. 2017; Cormier et al. 2018). Alternatively, high  $\mathcal{R}_{12/13}$  in a galactic region may indicate the presence of more diffuse molecular gas than in low  $\mathcal{R}_{12/13}$  regions (e.g. Rickard & Blitz 1985; Goldsmith et al. 2008; Pety et al. 2013; Roman-Duval et al. 2016). These findings suggest that changes in  $\mathcal{R}_{12/13}$  may reflect variations in the density of molecular gas in different regions within a galaxy.

On the other hand, variations in  $\mathcal{R}_{12/13}$  could reflect variations in  $^{13}\text{CO}$  abundance resulting from changes in the production or destruction of  $^{13}\text{C}$  or  $^{13}\text{CO}$ . While  $^{12}\text{C}$  is produced by all stars through various mass loss mechanisms,  $^{13}\text{C}$  is ejected into the ISM in the AGB phase of low mass stars mainly via CNO processing of  $^{12}\text{C}$ . The isotope fractional abundance  $[^{12}\text{C}/^{13}\text{C}]$  is therefore an important tracer of the chemical evolution of galaxies.  $[^{12}\text{C}/^{13}\text{C}]$  in nearby galaxies could range from 20 to 150 (Wilson & Rood 1994; Henkel et al. 2014; Tang et al. 2019, and references therein). Due to the high opacity of CO (typically  $> 1$  in extragalactic environments),  $\mathcal{R}_{12/13}$  sets a lower bound on  $[^{12}\text{C}/^{13}\text{C}]$  (Henkel & Mauersberger 1993; Henkel et al. 2014). Abnor-

mally high  $\mathcal{R}_{12/13}$  values are found in (U)LIRGs and high redshift galaxies and have been suggested to result from recent star formation in these galaxies (Danielson et al. 2013; Sliwa et al. 2017). Meanwhile, studies using chemical evolution modeling suggests  $\mathcal{R}_{12/13}$  could be used as a diagnostic of the stellar initial mass function (Romano et al. 2017; Zhang et al. 2018). In addition, chemical modeling studies suggest that the carbon fractionation in CO,  $[^{12}\text{CO}/^{13}\text{CO}]$ , is less affected by the ISM chemistry over long time scales and in typical physical conditions, thus making it a plausible tracer of primordial  $[^{12}\text{C}/^{13}\text{C}]$  in galactic environment (Viti et al. 2020; Colzi et al. 2020). Nonetheless, our overall understanding of how  $\mathcal{R}_{12/13}$  relates to the chemical evolution of galaxies remains poorly constrained, and may benefit from inclusion of stellar and gas metallicity data.

In this paper, we present a systematic study of  $^{13}\text{CO}(J = 1 \rightarrow 0)$  and  $\mathcal{R}_{12/13}$  variations down to kpc scales in the nearby universe, using the CARMA Extragalactic Database for Galaxy Evolution (EDGE) sample which targeted a total of 126 galaxies (Bolatto et al. 2017). Combining our  $^{12}\text{CO}$  and  $^{13}\text{CO}$  observations with optical spectroscopic data, we investigate how  $\mathcal{R}_{12/13}$  could be affected by global galaxy properties and how its variations relate to the underlying stellar population and ionized gas on kpc scales. Our systematic study of  $\mathcal{R}_{12/13}$  over a wide variety of galaxies could provide useful insights about molecular gas properties in response to local star formation activity, chemical evolution, and to large scale dynamical processes. We describe the  $^{13}\text{CO}$  observations and the ancillary data from the CALIFA IFU survey in Section 2. In Section 4, we present measurements of  $\mathcal{R}_{12/13}$  and relate them to global and resolved properties. We discuss the possible causes of  $\mathcal{R}_{12/13}$  variations and the caveats of this study in Section 5.

## 2. OBSERVATIONS AND DATA DESCRIPTION

### 2.1. EDGE $^{13}\text{CO}$ observations

$^{13}\text{CO}$  was simultaneously observed with  $^{12}\text{CO}$  in the EDGE survey. For the purpose of this study focusing on  $^{13}\text{CO}$ , we summarize the essential characteristics of  $^{13}\text{CO}$  observations. Full details of the survey, observations, and data reduction for the EDGE sample are described in Bolatto et al. (2017).

The observations of CARMA EDGE were carried out from late 2014 to mid 2015 in the CARMA D and E arrays. The targets are 126 galaxies from the CALIFA sample selected for high 22  $\mu\text{m}$  flux. The redshifted  $^{13}\text{CO}$  line, with a rest frequency of 110.201 GHz, is covered in the lower sideband (LSB). To cover a velocity range of 3800 km/s with 14.3 km/s resolution, the LSB

setup uses 3 spectral windows with bandwidth of 500 MHz each, whereas for  $^{12}\text{CO}$  the bandwidth is 250 MHz and 5 spectral windows are used for a combined velocity range of 3000 km/s. Therefore,  $^{13}\text{CO}$  has a lower spectral resolution of 14.3 km/s than the  $^{12}\text{CO}$  with 3.4 km/s resolution.

A 7-point hexagonal mosaic with centers separated by half the primary beam size of  $27''$  was used, to cover a field-of-view (FoV) with radius  $\sim 50''$ . The integration time of each galaxy is about 40 minutes in E-array, and  $\sim 3.5$  hours in D-array.

The visibility data were calibrated by the automatic pipeline developed for STING using MIRIAD (Rahman et al. 2011, 2012; Wong et al. 2013). The uncertainty of the flux calibration is estimated at  $\sim 10\%$  (see Bolatto et al. 2017 for details). The calibrated data were deconvolved and imaged using the MIRIAD tasks MOSSDI2 and INVERT with Briggs’s weighting robustness parameter of 0.5. The resulting typical beam size for  $^{13}\text{CO}$  is  $\sim 5''$ . Cubes were generated with a pixel size of  $1''$  and a velocity range is  $860 \text{ km s}^{-1}$  ( $1600 \text{ km s}^{-1}$  for Arp 220) with a channel spacing of  $20 \text{ km s}^{-1}$ .

We align the  $^{13}\text{CO}$  cube to match the pixel grid of the  $^{12}\text{CO}$  cube for each galaxy. We choose a common resolution of  $7''$  and smooth all the  $^{12}\text{CO}$  and  $^{13}\text{CO}$  cubes to a FWHM beam size of  $7''$  for further analysis. This resolution corresponds to physical scale of 0.68-4.4 kpc, given the range of distances of our sample is 20-130 Mpc. The typical channel noise for  $^{13}\text{CO}$  and  $^{12}\text{CO}$  at this resolution are 8.5 mK and 16.1 mK respectively.

## 2.2. Auxiliary Maps from EDGE-CALIFA

### 2.2.1. EDGE $^{12}\text{CO}$ Moment Maps

The  $^{12}\text{CO}$  integrated intensities are derived from their respective cubes after applying the  $^{12}\text{CO}$  dilated mask from Bolatto et al. (2017) in order to reject regions of the cube dominated by noise. The mask was generated by identifying pixels with  $^{12}\text{CO}$  emission above  $3.5\sigma$  in two adjacent channels of the cube, and expanding to contiguous regions with  $^{12}\text{CO}$  brightness above  $2\sigma$ . The mask was expanded by an additional “guard” band of 1 pixel in all three dimensions in order to capture additional low-level emission. The first three moments of the emission within the mask (moment-0, 1, and 2) were then calculated, representing the integrated intensity, intensity-weighted mean velocity, and intensity-weighted velocity dispersion respectively.

### 2.2.2. The CALIFA IFU Maps

The galaxies in the EDGE sample are selected from the CALIFA survey DR3, an optical IFU survey consisting of  $\sim 600$  nearby galaxies observed by the 3.5 m

telescope at the Calar Alto Observatory (Sánchez et al. 2012, 2016a). The spatial resolution of CALIFA is typically  $2.5''$ , corresponding to a scale of  $\sim 700$  pc at a distance of 64 Mpc (Bolatto et al. 2017). The spectra are observed in two settings, with a low resolution of  $6 \text{ \AA}$  across an unvignetted spectral range of 4240–7140  $\text{\AA}$  and a medium resolution of  $2.3 \text{ \AA}$  covering 3650–4620  $\text{\AA}$  (Sánchez et al. 2016a).

The spatially resolved properties of the stellar populations and emission lines are derived from the CALIFA observations by Pipe3D (Sánchez et al. 2016b). The Pipe3D data products are stored as maps with a pixel size of  $1''$  for each galaxy. Within Pipe3D, the resolved stellar mass, age, and metallicity are derived from the stellar populations modeling of the stellar emission. Fluxes, velocities, and line widths of the emission lines of each pixel are also derived by Pipe3D, and are used to derive the resolved ionized gas properties (Section 2.4.2).

## 2.3. Global Properties of Galaxies

### 2.3.1. $^{12}\text{CO}$ Velocity Dispersion

Although the  $^{12}\text{CO}$  moment-2 map provides a nominal estimate of the velocity dispersion at each location in the galaxy, it does not correct for the beam smearing of the galaxy’s rotation, which can be especially important in the central regions of galaxies where the velocity gradient is largest. We therefore obtained a separate estimate of the  $^{12}\text{CO}$  velocity dispersion as a function of radius by fitting a circular rotation model directly to the masked  $^{12}\text{CO}$  data cube, using the 3D-Barolo software package (Di Teodoro & Fraternali 2015). The fitting was performed with the center position fixed to the value provided by NED and with initial estimates of disk position angle (P.A.) and inclination provided by Levy et al. (2018). For roughly a dozen galaxies, the center was shifted to the  $^{12}\text{CO}$  intensity peak if a clearly defined peak was present and this resulted in smaller residuals and thus a substantially improved kinematic fit. The program runs in two stages, in which the systemic velocity and P.A. are allowed to vary with radius in the first stage, and are then fixed to their mean fitted values in the second stage. The rotation velocity and velocity dispersion are allowed to vary with radius in both stages. Up to 8 rings of width  $3''$  are fitted for each galaxy, although not all rings provide successful fits. We characterize the face-on velocity dispersion of each galaxy as the median value of the dispersion, obtained at the second fitting stage, for all rings in the galaxy.

### 2.3.2. Other Host Galaxy Properties

The Pipe3D data products are used to derive the global properties for each galaxy in CALIFA, either by

integrating or taking the characteristic values at the effective radius (Sánchez et al. 2018). The global stellar mass of galaxy ( $M_*$ ) is calculated by integrating all the pixels in the FoV with S/N > 1 in the continuum. The global SFR is also derived by integration. On the other hand, the global age, metallicity, and dust extinction are the corresponding mean values of the pixels at the effective radius  $r_e$ . In particular, the global age is the luminosity weighted age of the stellar population at  $r_e$ , the gas metallicity is derived using the Marino et al. (2013) O2N3 calibration (Equation 3) at  $r_e$ , and the global  $A_V$  is the dust attenuation in the  $V$  band derived from the  $H\alpha/H\beta$  line ratio at  $r_e$ . In addition, we obtain *IRAS* IR colors  $F_{60}/F_{100}$  from NED for each galaxy and list them in Table 1. Galaxy parameters such as distance,  $M_*$ , SFR, and metallicity for the EDGE-CALIFA survey can be found in Table 1 and 3 in Bolatto et al. (2017). The rest of the global parameters we use in this paper are presented in the Appendix.

Barrera-Ballesteros et al. (2015a) classified a sample of 103 CALIFA galaxies into different interacting stages using  $r$ -band Sloan Digital Sky Survey images. We use the stages they identified; for our sample that are not in these 103 galaxies, we classify the stage using the same method as in Barrera-Ballesteros et al. (2015a). For this study, we define a galaxy as “interacting” if it is in the merging stage (galaxy in a binary system with clear signatures of interaction) or post-merger stage (with the nuclei coalesced and evident tidal features) following Barrera-Ballesteros et al. (2015a).

## 2.4. Resolved Data Points

### 2.4.1. Data alignment and extraction

We align and convolve the CALIFA Pipe3D maps to match the EDGE CO maps and build a database that combines all the resolved properties of stars, ionized gas, and molecular gas. The Pipe3D maps are first regridded to the EDGE CO cubes using the IDL routine *hastrom* so that all the images of each galaxy are in the same celestial and velocity frame. Subsequently, we convolve the regridded Pipe3D maps to  $7''$  using a Gaussian kernel to match the typical resolution of the EDGE CO observations, assuming a Gaussian PSF of  $2.5''$  for the CALIFA cubes. We note this convolution is only correct for surface brightnesses, therefore properties such as SFR and metallicity are derived after smoothing following the methods described in Section 2.4.2.

After the CALIFA and EDGE images are aligned and smoothed, we extract values from both the regridded and smoothed images along a hexagonal sampling grid. We generate the hexagonal grid with a nearest-neighbor spacing of  $3.5''$ , that is, half of the FWHM beam size

of the convolved images. Pixel values in radio maps usually oversample the beam and hence are not independent; this resampling reduces the number of pixels by a factor of 10 while still preserving a modest degree of oversampling (from §3.1 there are 55 pixels per beam area compared to approximately 5 hexagonal grids per beam). We adopt a hexagonal grid because it leads to equal spacing between all adjacent pixels, and we expect that the adopted sampling scheme has negligible impact on our results. We take the values of the  $1'' \times 1''$  pixel nearest to each hexagonal grid point and extract them from the images for the analysis in this paper. Throughout the paper, we use the term “grids” to refer to the hexagonally sampled pixels to distinguish them from the original pixels of the maps.

### 2.4.2. Derived Resolved Properties

We calculate the star formation rate (SFR) from the extinction corrected  $H\alpha$  flux of each grid. The attenuation of  $H\alpha$  is calculated from the flux ratio of  $H\alpha/H\beta$  using Eq. (1) from Catalán-Torrecilla et al. (2015):

$$A(H\alpha) = \frac{K_{H\alpha}}{-0.4 \times (K_{H\alpha} - K_{H\beta})} \times \log \frac{H\alpha/H\beta}{2.86}, \quad (1)$$

where  $K_{H\alpha} = 2.53$ ,  $K_{H\beta} = 3.6$  are the extinction coefficients defined in Cardelli et al. (1989) for the Galactic extinction curve, and the constant 2.86 is the intrinsic Balmer ratio for case B recombination. After the extinction correction,  $H\alpha$  flux is converted to SFR following Eq. (2) from Rosa-González et al. (2002) assuming a Salpeter IMF:

$$SFR(M_\odot \text{ yr}^{-1}) = 7.9 \times 10^{-42} L_{H\alpha}(\text{erg s}^{-1}). \quad (2)$$

We use the Salpeter IMF for historical reasons related to CALIFA data processing (Sánchez et al. 2016b). For a more realistic SFR comparable to other recent values in the literature using IMF of Chabrier (2003) or Kroupa (2001), we suggest to divide the quoted value by  $\sim 1.6$  (Bolatto et al. 2017, and references therein).

Both of these equations used for the SFR calculations are applicable to star forming regions only. We therefore identify the star formation regions by applying the criterion suggested by Sánchez-Menguiano et al. (2016): we use the Kewley et al. (2001) demarcation line to exclude AGN-like regions, and require an  $H\alpha$  equivalent width of  $EW(H\alpha) > 6 \text{ \AA}$  to exclude weak AGNs and regions ionized by low-mass evolved stars (Cid Fernandes et al. 2011). Only for the grids classified as star forming regions is the star formation rate calculated using Equations (1) and (2). The surface densities are deprojected for disk inclination  $i$  using a correction factor of  $\cos i$  where  $i$  is tabulated in Bolatto et al. (2017) Table 1.

We also calculate the oxygen abundance  $12 + \log(\text{O}/\text{H})$  for each star forming grid from the O3N2 index,  $\text{O3N2} = \log([\text{OIII}]\lambda 5007/\text{H}\beta) - \log([\text{NII}]\lambda 6583/\text{H}\alpha)$ . We use the empirical relation calibrated from  $T_e$ -based abundance measurements by Marino et al. (2013):

$$12 + \log(\text{O}/\text{H}) = 8.53 - 0.21 \times \text{O3N2}. \quad (3)$$

Besides SFR and oxygen abundance, the remaining IFU-based resolved properties (stellar surface density, stellar mass metallicity, and dust extinction) used in this study are derived by Pipe3D directly, and are hence at the native CALIFA resolution and gridding.

### 2.5. Azimuthally averaged IFU properties

We derive azimuthally averaged stellar and ionised gas properties based on the corresponding resolved IFU maps. We use normalized radial bins  $r_{\text{gal}}/r_{25}$  with a step of 0.1. These values are used in Section 4.4 to investigate the correlations between azimuthally stacked line ratio  $\mathcal{R}_{12/13}^{\text{stack}}$  and local properties. Since  $\mathcal{R}_{12/13}^{\text{stack}}$  are measured from the stacked spectra which average the CO emissions for a given radial bin (see Section 3.3), we use the mean value of each property to represent the bin, except for the sSFR, molecular gas fraction, and ionized metallicity because these are ratios. For the sSFR and molecular gas fraction, we use the mean values of stellar surface density, star formation surface density, and the molecular gas surface density to derive the corresponding ratios for the radial bin. For the ionized metallicity, we choose the median of resolved  $12 + \log(\text{O}/\text{H})$  to represent the annulus instead of the mean.

## 3. $^{13}\text{CO}$ MEASUREMENTS

### 3.1. $^{13}\text{CO}$ Moment-0 Maps

We use the same  $^{12}\text{CO}$  dilated mask from Bolatto et al. (2017) to generate the  $^{13}\text{CO}$  integrated intensity maps. We detect resolved  $^{13}\text{CO}$  intensity  $I_{13}$  in 30 galaxies (Figure 1); in each of these galaxies, there are more than 27 pixels (corresponding to half the size of a Gaussian beam of  $7''$ ) detected in  $^{13}\text{CO}$  with  $\text{S}/\text{N} > 4$ . Since  $^{12}\text{CO}$  masks are used to derive the  $^{13}\text{CO}$  maps, negative values are occasionally present especially in the outer disks, mainly due to the random noise fluctuations of the faint  $^{13}\text{CO}$  emission. All galaxies with  $I_{13}$  detected are also considered detections in integrated flux of  $^{13}\text{CO}$  ( $F_{13}$ , see Section 3.2), except for IC 0480 and UGC 04029. In these two galaxies,  $^{13}\text{CO}$  is well detected in galaxy centers. However, the overall  $^{13}\text{CO}$  emission is weak; negative  $^{13}\text{CO}$  fluxes from the noisy regions on the edges of the maps diminish  $F_{13}$  integrated in both velocity and position below the detection limit.

The  $^{13}\text{CO}$  intensity maps of the 30 galaxies with resolved  $I_{13}$  detected are shown in Figure 1. Because  $^{13}\text{CO}$  is much weaker and has lower S/N than  $^{12}\text{CO}$  in our observations,  $^{13}\text{CO}$  intensity ( $I_{13}$ ) detections with  $\text{S}/\text{N} > 4$  (shown in the black contours) are mostly located within regions with brightest  $^{12}\text{CO}$ . Regions where we have reliable resolved  $I_{13}$  and  $\mathcal{R}_{12/13}$  are very limited and biased. Therefore, to capture the more robust averaged features, we stack the spectra over multiple regions/grids (see Section 3.3).

### 3.2. $^{13}\text{CO}$ Flux Spectra

We sum all of the  $^{12}\text{CO}$  and  $^{13}\text{CO}$  spectra within the  $^{12}\text{CO}$  dilated mask to obtain integrated spectra for each galaxy. In other words, the flux in each channel is the summed intensity for all valid pixels in the mask. We also calculate velocity-integrated  $^{12}\text{CO}$  and  $^{13}\text{CO}$  fluxes ( $F_{12}$  and  $F_{13}$ ) from these masked spectra. The uncertainty in the spectra and fluxes are calculated by error propagation, taking into account the oversampling of the beam and using root-mean-square (RMS) noise values estimated from the signal-free velocity channels.

We list in Table 1 the galaxy properties and  $^{13}\text{CO}$  fluxes of the 41 galaxies with  $\text{S}/\text{N}(F_{13}) > 4$ . The other 64 galaxies detected in  $F_{12}$  but not  $F_{13}$  are still used to provide lower limits on the galaxy integrated line ratio  $\mathcal{R}_{12/13}^{\text{gal}}$  in the investigation of global correlations (Figure 4). We provide the upper limits of  $F_{13}$  and the lower limit of  $\mathcal{R}_{12/13}^{\text{gal}}$  for these galaxies in Table 1. The remaining 21 galaxies in the EDGE-CALIFA sample are not detected in  $F_{12}$  at the  $3\text{-}\sigma$  level, and we omit these galaxies in the rest of the paper. The  $^{13}\text{CO}$  and  $^{12}\text{CO}$  flux spectra of the 56  $F_{13}$  detected galaxies are shown in Figure 2. We note that because the mask is a function of velocity, the specific flux and its uncertainty at a given channel depends strongly on the emission mask. The  $\pm 1\sigma$  uncertainties in the  $^{13}\text{CO}$  spectra are indicated by the blue shading in Figure 2.

### 3.3. Radial stacked $^{13}\text{CO}$ spectra

Since both  $I_{12}$  and  $I_{13}$  generally decrease exponentially with radius, few individual grids at large radius have detectable  $I_{13}$ , leaving parts of the parameter space unexplored in our resolved study of  $\mathcal{R}_{12/13}$ . To improve the S/N compared to what can be achieved in individual grids, we first deproject the position of each grid on to the galactic plane using the galaxy's inclination and position angle, and calculate its distance to the galaxy's center  $r_{\text{gal}}$ . We then obtain the radial profiles of  $\mathcal{R}_{12/13}$  by stacking the spectra of  $I_{12}$  and  $I_{13}$  in normalized radial bins in units of  $r_{\text{gal}}/r_{25}$ . In a given radial bin, the  $^{13}\text{CO}$  and  $^{12}\text{CO}$  spectra for all the grids with  $I_{12}$  detected are selected. All of the masked spectra in the

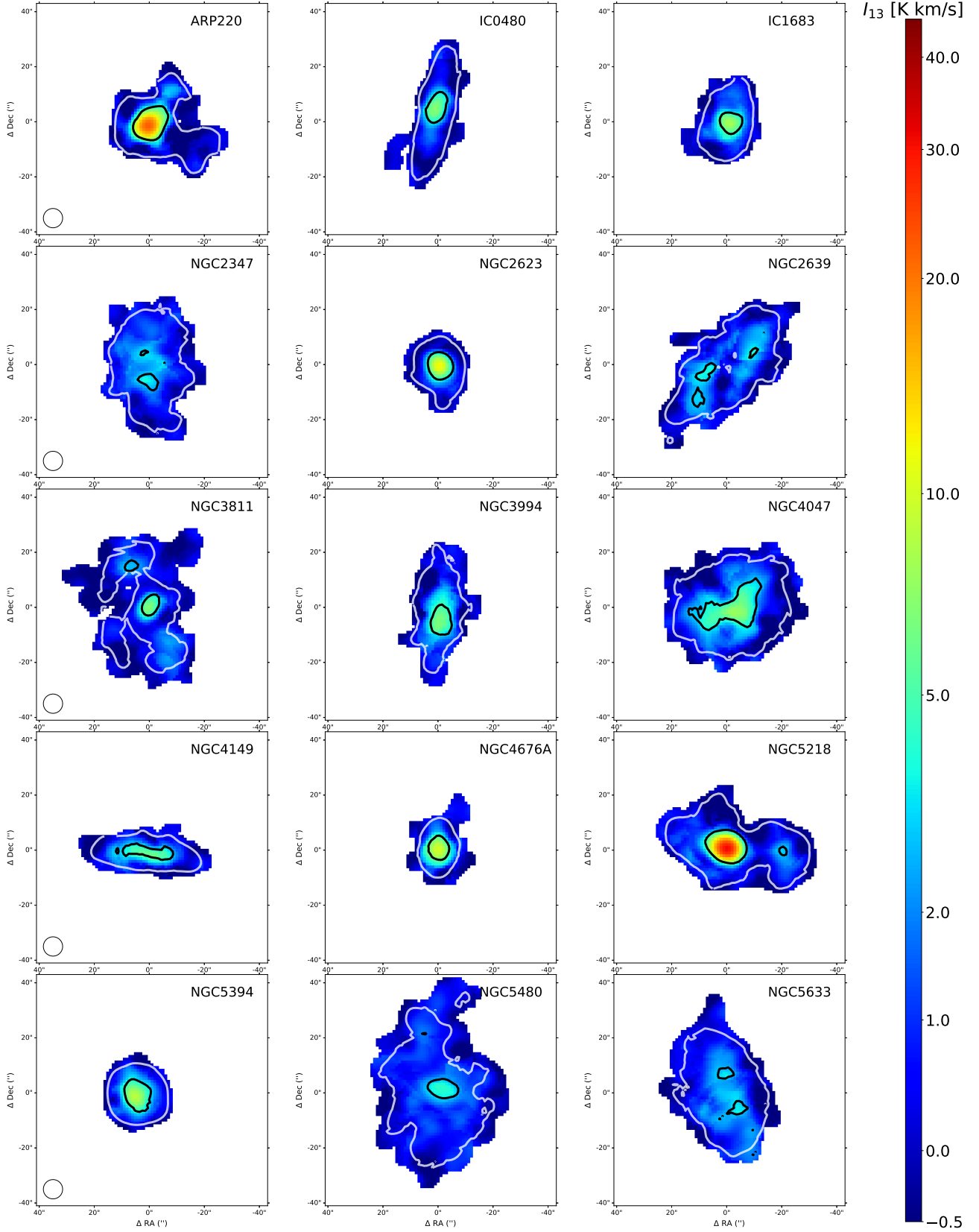


**Figure 1.**  $^{13}\text{CO}$  intensity maps of the 30 galaxies with resolved  $^{13}\text{CO}$  detected from the EDGE survey. The black contours overlaid show the  $^{13}\text{CO}$  intensity observed with  $S/N > 4$ , while the white contours levels show the  $^{12}\text{CO}$  intensity with  $S/N > 3$ . The black circles in the first panel of each row show the beam size. We use a single color palette for all the galaxies, and the color scale is adjusted to emphasize the  $^{13}\text{CO}$  emission.

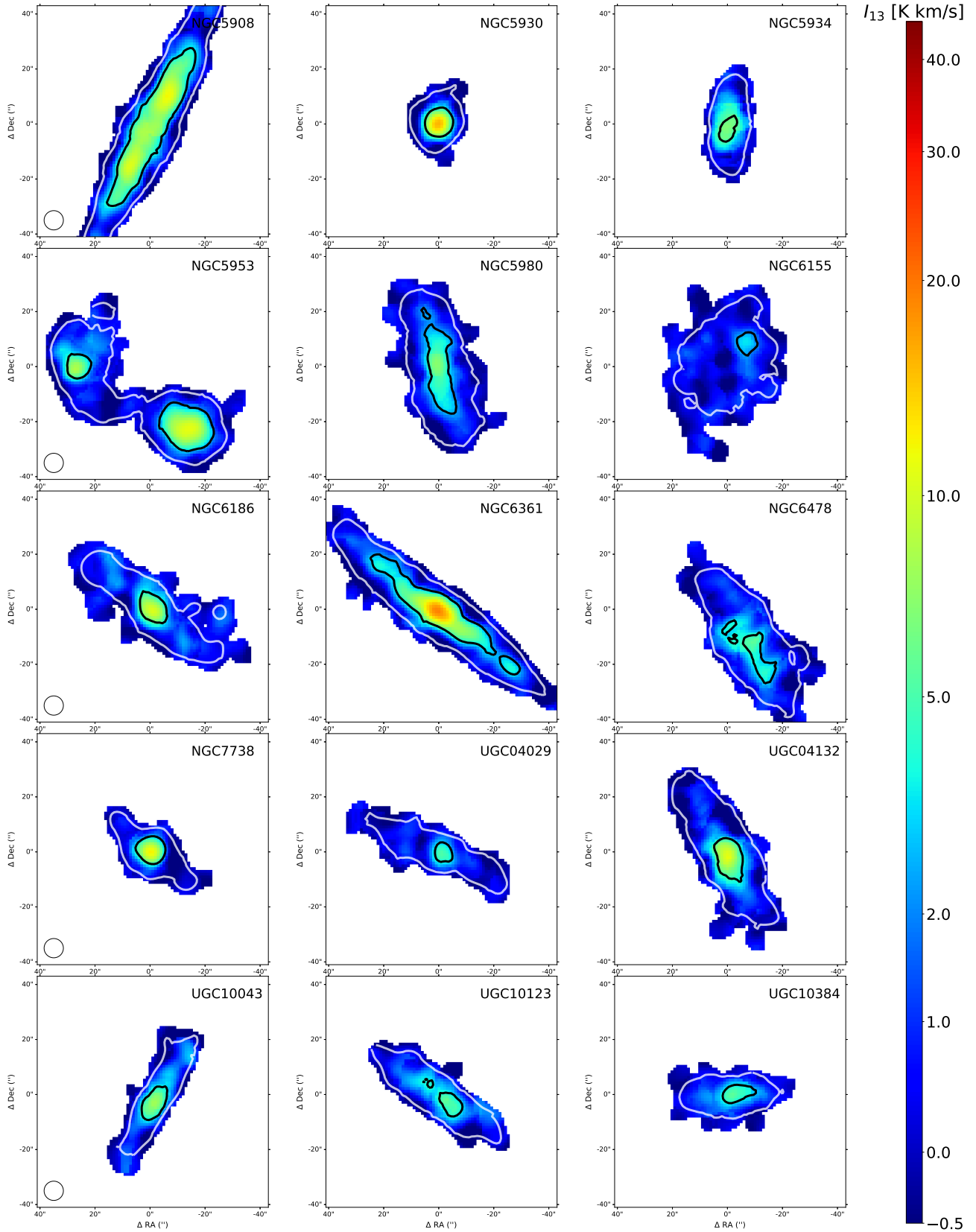
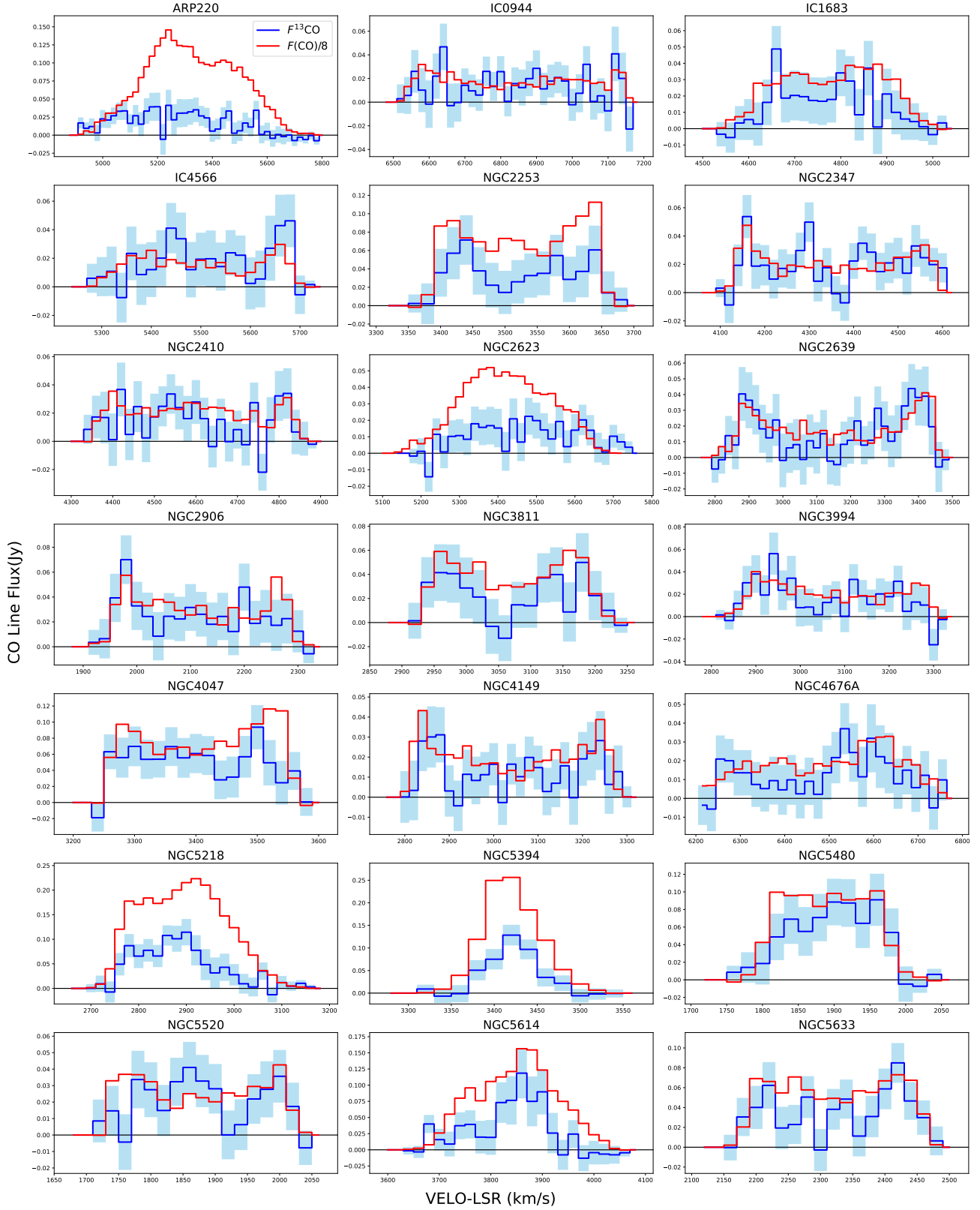


Figure 1. (Continued).



**Figure 2.**  $^{13}\text{CO}$  flux spectra for the 41 galaxies with  $F_{13}$  detected. The blue lines show the  $^{13}\text{CO}$  flux in each channel obtained using the dilated  $^{12}\text{CO}$  masks, and red lines are the  $^{12}\text{CO}$  flux resulting from the same masks scaled down by a factor of 8. The light blue shaded regions represent  $1\sigma$  uncertainty of  $^{13}\text{CO}$  flux.



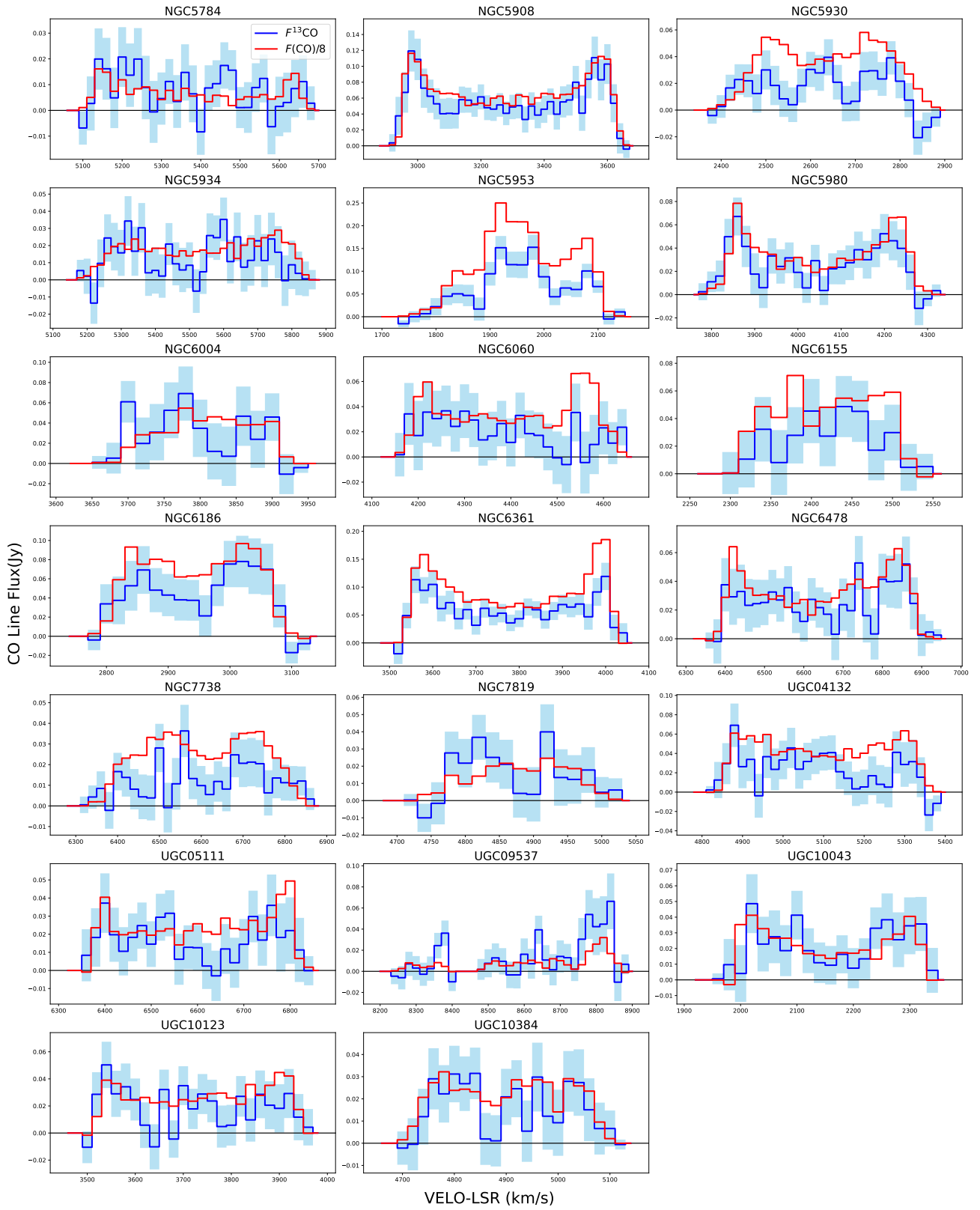


Figure 2. (Continued).

radial bin are shifted to a common central velocity (the weighted mean velocity of the  $^{12}\text{CO}$  line provided by

the moment-1 map), and are then averaged. The channel noise of the stacked spectrum is calculated by taking

the RMS of all the spectra that are stacked, and then scaling by a factor of  $\sqrt{5.23}$  to account for the oversampling rate of 5.23 of the hexagonal grids. We fit the stacked  $^{12}\text{CO}$  and  $^{13}\text{CO}$  spectra with a Gaussian function, and obtain the integrated fluxes from the Gaussian integral. The uncertainty of the integrated flux is calculated by

$$\epsilon_{\text{stack}} = \sigma_{\text{ch}} \sqrt{\text{FWHM} \cdot \Delta V_{\text{ch}}}. \quad (4)$$

where  $\sigma_{\text{ch}}$  and  $\Delta V_{\text{ch}}$  are the channel noise and the channel width of the stacked spectrum respectively, and FWHM is obtained from the Gaussian fitting.

We start from the initial radial bins with a step of  $0.1(r_{\text{gal}}/r_{25})$ . If the stacked  $^{13}\text{CO}$  integrated flux  $I_{13}^{\text{stack}}$  is below the detection threshold of  $S/N = 4$ , we merge the bin with the next in the direction of increasing  $r_{\text{gal}}$ , until  $I_{13}^{\text{stack}}$  has  $S/N > 4$ , the bin size reaches an upper

limit of  $0.4(r_{\text{gal}}/r_{25})$ , or there are no more bins to merge beyond  $0.8(r_{\text{gal}}/r_{25})$ , and repeat the stacking. We show the stacked spectra of two galaxies as examples in Appendix C. The Gaussian fitted fluxes resulting from the stacked  $^{12}\text{CO}$  and  $^{13}\text{CO}$  spectra in these adjusted bins are used to derive the radial profiles of stacked line ratio  $\mathcal{R}_{12/13}^{\text{stack}}$  (see Section 4.3).

In total, we detect  $I_{13}^{\text{stack}}$  in 41 galaxies in our sample. All of the galaxies with resolved  $I_{13}$  detected are also detected with the spectral stacking method, except for the five galaxies for which we adopt inclinations of  $90^\circ$  (IC0480, UGC04029, UGC10043, UGC10123, UGC10384). For these galaxies, the galactic distance  $r_{\text{gal}}$  cannot be calculated, so we omit them from the azimuthal stacking.

**Table 1.**  $^{13}\text{CO}$  and  $\mathcal{R}_{12/13}$  measurements in the EDGE-CALIFA Survey

Galaxy	$F_{13}$	$\mathcal{R}_{12/13}^{\text{gal}}$	$\langle\sigma(I_{13})\rangle$	$\mathcal{N}_{13}$	$\mathcal{N}_{12}$	$\mathcal{N}_{12}^{\mathcal{R}}$	$\mathcal{R}_{12/13}$	$\mathcal{N}_{13}^{\text{stack}}$	$\mathcal{R}_{12/13}^{\text{stack}}$	$F_{60}/F_{100}$	Inter	Bar
	(Jy km/s)		(K km/s)									
(1)	(2)	(3)	(4)	(5)	(6)	(7)	(8)	(9)	(10)	(11)	(12)	(13)
ARP220	$14.1 \pm 1.9$	$29.0 \pm 3.9$	0.8	10	11	68	$25.7 \pm 4.9$	2	$27.7 \pm 2.7$	$0.903 \pm 0.001$	1	0
IC0480	$\leq 5.1$	$\geq 14.0$	0.7	6	0	47	$7.8 \pm 1.2$	0	...	$0.43 \pm 0.04$	0	0
IC0540	$\leq 3.7$	$\geq 5.2$	0.7	0	3	12	...	0	...	$0.24 \pm 0.04$	0	0
IC0944	$8.4 \pm 1.8$	$9.8 \pm 2.2$	0.7	0	2	71	...	3	$7.7 \pm 1.8$	$0.23 \pm 0.03$	0	0
IC1199	$\leq 4.8$	$\geq 8.5$	0.6	0	0	59	...	0	...	$0.36 \pm 0.07$	0	0
IC1683	$6.6 \pm 1.3$	$12.5 \pm 2.5$	0.7	4	5	43	$10.4 \pm 2.3$	2	$11.6 \pm 1.7$	$0.50 \pm 0.05$	0	0
IC2247	$\leq 4.5$	$\geq 14.3$	0.5	0	0	61	...	0	...	$0.38 \pm 0.04$	0	0
IC2487	$\leq 5.4$	$\geq 9.1$	0.6	0	0	55	...	0	...	$0.32 \pm 0.04$	0	0
IC4566	$7.7 \pm 1.7$	$6.2 \pm 1.4$	0.7	0	0	81	...	0	...	$1.0 \pm 1.4$	0	1
IC5376	$\leq 2.6$	$\geq 2.9$	0.6	0	0	12	...	0	...	$1.0 \pm 1.4$	0	0
NGC0447	$\leq 4.4$	$\geq 7.2$	0.6	0	2	30	...	0	...	$1.0 \pm 1.4$	0	1
NGC0477	$\leq 6.6$	$\geq 5.0$	0.7	0	0	50	...	0	...	$0.32 \pm 0.05$	0	1
NGC0496	$\leq 5.2$	$\geq 7.2$	0.6	0	0	52	...	1	$8.4 \pm 2.1$	$0.30 \pm 0.05$	0	0
NGC0523	$\leq 6.9$	$\geq 13.3$	0.7	0	0	71	...	0	...	$0.44 \pm 0.05$	1	0
NGC0551	$\leq 5.3$	$\geq 6.9$	0.5	0	0	78	...	0	...	$0.28 \pm 0.04$	0	1
NGC1167	$\leq 4.4$	$\geq 3.4$	0.6	0	0	16	...	0	...	$0.11 \pm 0.03$	0	0
NGC2253	$10.8 \pm 2.0$	$14.0 \pm 2.6$	0.6	0	1	144	...	3	$14.4 \pm 3.1$	$0.40 \pm 0.03$	0	0
NGC2347	$10.0 \pm 1.4$	$7.7 \pm 1.1$	0.5	4	0	90	$6.2 \pm 1.1$	3	$7.6 \pm 1.8$	$0.36 \pm 0.03$	0	0
NGC2410	$7.7 \pm 1.6$	$10.2 \pm 2.2$	0.6	0	0	86	...	2	$9.4 \pm 1.5$	$0.41 \pm 0.03$	0	1
NGC2480	$\leq 2.6$	$\geq 4.7$	0.5	0	0	16	...	0	...	$1.0 \pm 1.4$	1	1
NGC2487	$\leq 7.6$	$\geq 6.5$	0.7	0	1	47	...	0	...	$0.21 \pm 0.03$	0	1
NGC2623	$5.7 \pm 1.0$	$19.7 \pm 3.6$	0.7	5	4	31	$15.5 \pm 2.0$	2	$14.4 \pm 2.1$	$0.917 \pm 0.004$	1	0
NGC2639	$10.3 \pm 1.8$	$8.8 \pm 1.6$	0.7	5	0	93	$3.7 \pm 1.2$	2	$7.4 \pm 0.9$	$0.28 \pm 0.02$	0	0
NGC2730	$\leq 5.9$	$\geq 4.8$	0.5	0	0	27	...	0	...	$0.40 \pm 0.05$	0	1
NGC2906	$9.7 \pm 1.7$	$8.7 \pm 1.5$	0.6	0	0	99	...	4	$7.8 \pm 1.5$	$0.34 \pm 0.03$	0	0
NGC2916	$\leq 5.9$	$\geq 4.6$	0.7	0	0	34	...	0	...	$0.28 \pm 0.03$	0	0
NGC3303	$\leq 5.2$	$\geq 5.8$	0.9	0	5	25	...	0	...	$1.0 \pm 1.4$	1	0
NGC3381	$\leq 3.4$	$\geq 4.2$	0.5	0	0	15	...	0	...	$0.36 \pm 0.03$	0	1
NGC3811	$6.9 \pm 1.7$	$12.2 \pm 3.1$	0.6	3	2	80	$8.9 \pm 2.3$	3	$9.1 \pm 2.2$	$0.44 \pm 0.44$	0	1
NGC3815	$\leq 5.2$	$\geq 8.0$	0.7	0	0	48	...	1	$8.1 \pm 1.8$	$0.44 \pm 0.44$	0	0

**Table 1** *continued*

Table 1 (*continued*)

Galaxy	$F_{13}$	$\mathcal{R}_{12/13}^{\text{gal}}$	$\langle\sigma(I_{13})\rangle$	$\mathcal{N}_{13}$	$\mathcal{N}_{12}$	$\mathcal{N}_{12}^{\text{R}}$	$\mathcal{R}_{12/13}$	$\mathcal{N}_{13}^{\text{stack}}$	$\mathcal{R}_{12/13}^{\text{stack}}$	$F_{60}/F_{100}$	Inter	Bar
	(Jy km/s)		(K km/s)									
(1)	(2)	(3)	(4)	(5)	(6)	(7)	(8)	(9)	(10)	(11)	(12)	(13)
NGC3994	$7.8 \pm 1.5$	$9.2 \pm 1.8$	0.7	6	3	52	$5.8 \pm 1.0$	1	$9.4 \pm 2.3$	$0.48 \pm 0.07$	0	0
NGC4047	$16.9 \pm 2.0$	$10.6 \pm 1.3$	0.7	21	6	118	$7.0 \pm 1.5$	4	$8.4 \pm 1.0$	$0.36 \pm 0.18$	0	0
NGC4149	$6.2 \pm 1.3$	$11.5 \pm 2.4$	0.7	6	3	39	$8.7 \pm 1.9$	1	$8.8 \pm 1.5$	$0.38 \pm 0.03$	0	1
NGC4185	$\leq 4.2$	$\geq 2.8$	0.7	0	0	14	...	0	...	...	0	1
NGC4210	$\leq 6.0$	$\geq 7.5$	0.5	0	0	83	...	0	...	$0.24 \pm 0.03$	0	1
NGC4211N	$\leq 3.7$	$\geq 4.5$	0.8	0	3	12	...	0	...	$0.55 \pm 0.10$	1	0
NGC4470	$\leq 5.1$	$\geq 6.4$	0.6	0	0	45	...	0	...	$0.43 \pm 0.02$	0	0
NGC4644	$\leq 4.0$	$\geq 6.8$	0.5	0	0	48	...	0	...	$1.0 \pm 1.4$	0	1
NGC4676A	$6.7 \pm 1.4$	$10.5 \pm 2.3$	0.9	5	7	24	$9.2 \pm 2.3$	1	$9.4 \pm 1.5$	$0.52 \pm 0.04$	1	1
NGC4711	$\leq 5.3$	$\geq 7.0$	0.6	0	0	58	...	1	$7.8 \pm 2.0$	$0.30 \pm 0.04$	0	1
NGC4961	$\leq 3.6$	$\geq 5.6$	0.5	0	0	34	...	0	...	$0.36 \pm 0.07$	0	1
NGC5000	$\leq 5.1$	$\geq 8.0$	0.6	0	3	39	...	0	...	$0.40 \pm 0.05$	0	1
NGC5016	$\leq 6.1$	$\geq 10.2$	0.6	0	0	81	...	2	$8.6 \pm 1.4$	$0.37 \pm 0.01$	0	1
NGC5056	$\leq 5.2$	$\geq 7.3$	0.6	0	0	60	...	0	...	$0.41 \pm 0.05$	0	0
NGC5205	$\leq 4.4$	$\geq 5.0$	0.6	0	0	28	...	0	...	$0.30 \pm 0.05$	0	0
NGC5218	$19.3 \pm 2.1$	$19.7 \pm 2.2$	0.7	13	12	101	$14.4 \pm 1.8$	3	$18.1 \pm 1.9$	$0.518 \pm 0.004$	1	1
NGC5394	$8.0 \pm 1.2$	$19.2 \pm 3.0$	0.8	7	8	39	$19.1 \pm 4.3$	3	$18.7 \pm 3.1$	$0.54 \pm 0.21$	1	1
NGC5406	$\leq 8.5$	$\geq 6.7$	0.7	0	0	73	...	0	...	$0.31 \pm 0.04$	0	1
NGC5480	$13.3 \pm 1.8$	$9.4 \pm 1.3$	0.6	6	0	127	$7.1 \pm 1.3$	5	$9.1 \pm 1.5$	$0.34 \pm 0.02$	0	0
NGC5520	$6.6 \pm 1.3$	$9.1 \pm 1.8$	0.6	0	0	56	...	2	$7.9 \pm 1.0$	$0.40 \pm 0.03$	0	0
NGC5614	$12.3 \pm 2.3$	$16.9 \pm 3.2$	0.8	0	4	109	...	2	$15.4 \pm 3.3$	$0.25 \pm 0.02$	1	0
NGC5633	$11.6 \pm 1.6$	$10.6 \pm 1.5$	0.6	4	0	97	$6.8 \pm 1.2$	5	$9.3 \pm 1.6$	$0.35 \pm 0.01$	0	0
NGC5657	$\leq 5.1$	$\geq 5.2$	0.9	0	4	20	...	0	...	$0.59 \pm 0.05$	0	1
NGC5732	$\leq 3.9$	$\geq 4.2$	0.6	0	0	22	...	0	...	$0.28 \pm 0.03$	0	0
NGC5784	$4.6 \pm 1.1$	$6.5 \pm 1.7$	0.6	0	0	35	...	0	...	$0.27 \pm 0.01$	0	0
NGC5908	$41.9 \pm 2.4$	$8.5 \pm 0.5$	0.8	52	53	132	$7.4 \pm 0.9$	4	$8.5 \pm 1.2$	$0.25 \pm 0.25$	0	0
NGC5930	$7.8 \pm 1.3$	$15.8 \pm 2.6$	0.8	7	7	30	$12.3 \pm 2.1$	2	$13.2 \pm 1.6$	$0.68 \pm 0.01$	1	1
NGC5934	$8.5 \pm 1.6$	$9.7 \pm 1.8$	0.9	4	9	41	$9.2 \pm 1.6$	1	$9.1 \pm 2.0$	$0.34 \pm 0.02$	1	0
NGC5947	$\leq 3.2$	$\geq 3.1$	0.5	0	0	21	...	0	...	$0.36 \pm 0.05$	0	1
NGC5953	$24.5 \pm 1.9$	$13.3 \pm 1.0$	0.6	31	25	128	$11.5 \pm 1.6$	4	$12.4 \pm 1.5$	$0.59 \pm 0.01$	1	0
NGC5980	$13.7 \pm 1.5$	$9.2 \pm 1.0$	0.6	22	3	101	$6.2 \pm 1.1$	5	$6.6 \pm 1.0$	$0.41 \pm 0.03$	0	0
NGC6004	$7.9 \pm 1.9$	$7.7 \pm 1.9$	0.6	0	0	74	...	2	$7.2 \pm 1.3$	$0.31 \pm 0.02$	0	1
NGC6060	$9.7 \pm 2.1$	$12.5 \pm 2.7$	0.6	0	0	158	...	2	$8.5 \pm 1.1$	$0.31 \pm 0.04$	0	1
NGC6155	$6.0 \pm 1.5$	$12.2 \pm 3.0$	0.5	4	0	104	$3.9 \pm 0.8$	3	$11.0 \pm 2.2$	$0.35 \pm 0.02$	0	0
NGC6168	$\leq 5.6$	$\geq 4.8$	0.7	0	0	38	...	0	...	$0.41 \pm 0.04$	0	0
NGC6186	$14.7 \pm 1.9$	$10.2 \pm 1.3$	0.7	7	11	76	$10.9 \pm 1.7$	5	$11.8 \pm 2.6$	$0.43 \pm 0.03$	0	1
NGC6301	$\leq 7.6$	$\geq 7.1$	0.7	0	0	110	...	1	$6.0 \pm 1.5$	$0.21 \pm 0.03$	0	0
NGC6310	$\leq 2.8$	$\geq 2.8$	0.6	0	0	13	...	0	...	$0.24 \pm 0.04$	0	0
NGC6314	$\leq 4.6$	$\geq 6.6$	0.6	0	2	36	...	0	...	...	0	0
NGC6361	$31.6 \pm 2.0$	$10.9 \pm 0.7$	0.7	39	36	124	$8.8 \pm 1.9$	7	$10.0 \pm 1.2$	$0.31 \pm 0.01$	0	0
NGC6394	$\leq 6.1$	$\geq 5.7$	0.8	0	0	42	...	0	...	$0.36 \pm 0.03$	0	1
NGC6478	$13.8 \pm 1.8$	$9.6 \pm 1.3$	0.7	12	3	101	$6.4 \pm 1.2$	4	$8.3 \pm 1.3$	$0.28 \pm 0.02$	0	0
NGC7738	$6.5 \pm 1.1$	$13.9 \pm 2.2$	0.6	8	6	40	$11.2 \pm 1.5$	3	$11.2 \pm 1.7$	$0.58 \pm 0.07$	0	1
NGC7819	$4.5 \pm 1.0$	$6.6 \pm 1.6$	0.6	0	2	27	...	2	$6.3 \pm 1.2$	$0.43 \pm 0.05$	0	1
UGC00809	$\leq 2.0$	$\geq 2.7$	0.5	0	0	9	...	0	...	...	0	0
UGC03253	$\leq 3.3$	$\geq 3.9$	0.6	0	0	16	...	0	...	$0.30 \pm 0.05$	0	1
UGC03539	$\leq 5.4$	$\geq 9.5$	0.7	0	0	41	...	0	...	$0.40 \pm 0.07$	0	1
UGC03969	$\leq 6.5$	$\geq 6.5$	0.8	0	0	43	...	1	$5.2 \pm 1.3$	$0.42 \pm 0.06$	0	0
UGC03973	$\leq 5.8$	$\geq 5.2$	0.7	0	0	48	...	0	...	$0.64 \pm 0.07$	0	1
UGC04029	$\leq 4.7$	$\geq 10.9$	0.6	3	0	55	$7.1 \pm 1.4$	0	...	$0.43 \pm 0.04$	0	1
UGC04132	$12.8 \pm 2.1$	$13.1 \pm 2.2$	0.8	10	7	90	$6.7 \pm 0.9$	4	$11.1 \pm 2.2$	$0.38 \pm 0.04$	0	0

Table 1 (*continued*)

Table 1 (continued)

Galaxy	$F_{13}$	$\mathcal{R}_{12/13}^{\text{gal}}$	$\langle\sigma(I_{13})\rangle$	$\mathcal{N}_{13}$	$\mathcal{N}_{12}$	$\mathcal{N}_{12}^{\mathcal{R}}$	$\mathcal{R}_{12/13}$	$\mathcal{N}_{13}^{\text{stack}}$	$\mathcal{R}_{12/13}^{\text{stack}}$	$F_{60}/F_{100}$	Inter	Bar
	(Jy km/s)		(K km/s)									
(1)	(2)	(3)	(4)	(5)	(6)	(7)	(8)	(9)	(10)	(11)	(12)	(13)
UGC04280	$\leq 3.3$	$\geq 3.9$	0.7	0	1	13	...	0	...	$0.44 \pm 0.07$	0	0
UGC04461	$\leq 4.5$	$\geq 6.5$	0.7	0	2	31	...	0	...	$0.43 \pm 0.05$	0	0
UGC05108	$\leq 4.3$	$\geq 5.7$	0.7	0	2	20	...	0	...	$0.48 \pm 0.07$	0	1
UGC05111	$8.2 \pm 1.4$	$10.1 \pm 1.8$	0.6	0	0	69	...	0	...	$0.28 \pm 0.08$	0	0
UGC05359	$\leq 3.3$	$\geq 3.2$	0.5	0	0	24	...	0	...	$1.0 \pm 1.4$	0	1
UGC05598	$\leq 4.5$	$\geq 4.1$	0.8	0	0	19	...	0	...	$0.34 \pm 0.05$	0	0
UGC07012	$\leq 2.6$	$\geq 3.1$	0.5	0	0	11	...	0	...	$1.0 \pm 1.4$	0	1
UGC08107	$\leq 6.8$	$\geq 10.8$	0.8	0	2	56	...	0	...	$0.28 \pm 0.05$	1	1
UGC08267	$\leq 5.6$	$\geq 8.2$	0.8	0	2	35	...	0	...	$0.27 \pm 0.05$	0	0
UGC09067	$\leq 6.3$	$\geq 6.6$	0.9	0	0	41	...	0	...	$0.38 \pm 0.06$	0	0
UGC09476	$\leq 6.8$	$\geq 6.4$	0.6	0	0	58	...	0	...	$0.29 \pm 0.03$	0	1
UGC09537	$8.3 \pm 1.7$	$4.3 \pm 0.9$	0.8	0	0	52	...	0	...	$0.28 \pm 0.04$	0	0
UGC09542	$\leq 4.8$	$\geq 5.5$	0.6	0	0	41	...	0	...	$0.21 \pm 0.03$	0	0
UGC09665	$\leq 5.3$	$\geq 10.6$	0.7	0	0	53	...	0	...	$0.36 \pm 0.03$	0	0
UGC09759	$\leq 4.9$	$\geq 8.6$	0.7	0	3	30	...	1	$8.3 \pm 1.7$	$0.29 \pm 0.03$	0	0
UGC09873	$\leq 2.8$	$\geq 3.4$	0.6	0	0	11	...	0	...	$1.0 \pm 1.4$	0	0
UGC09892	$\leq 3.7$	$\geq 4.4$	0.6	0	0	31	...	0	...	$1.0 \pm 1.4$	0	0
UGC09919	$\leq 2.2$	$\geq 2.4$	0.6	0	0	6	...	0	...	$0.35 \pm 0.08$	0	0
UGC10043	$8.4 \pm 1.4$	$7.1 \pm 1.2$	0.7	7	5	45	$4.4 \pm 0.9$	0	...	$0.34 \pm 0.03$	0	0
UGC10123	$8.9 \pm 1.6$	$10.0 \pm 1.8$	0.8	7	0	62	$5.8 \pm 1.6$	0	...	$0.32 \pm 0.02$	0	0
UGC10205	$\leq 5.6$	$\geq 6.0$	0.8	0	0	39	...	0	...	$0.26 \pm 0.05$	1	0
UGC10380	$\leq 4.8$	$\geq 3.3$	0.8	0	4	13	...	0	...	...	0	0
UGC10384	$6.8 \pm 1.2$	$9.3 \pm 1.7$	0.6	5	2	41	$8.0 \pm 1.8$	0	...	$0.41 \pm 0.04$	0	0
UGC10710	$\leq 6.1$	$\geq 5.4$	0.8	0	1	33	...	0	...	$0.21 \pm 0.04$	0	0

NOTE— (1) Galaxy name; (2)  $^{13}\text{CO}$  integrated flux or its upper limit; (3) Integrated (global)  $^{12}\text{CO}$ -to- $^{13}\text{CO}$  line ratio or its lower limit; (4) The mean  $1\sigma$  noise of resolved  $I_{13}$  using the dilated  $^{12}\text{CO}$  mask. (5) Number of hexagon grids with resolved  $I_{13}$  detected with  $S/N > 4$ ; (6) Number of hexagon grids with resolved  $I_{12}$  detected with  $S/N > 3$ ; (7) Number of hexagon grids with resolved  $I_{12}$  that are  $\mathcal{R}_{12/13}^{\text{gal}}$  times brighter than the  $I_{13}$  detection threshold; (8) Median of resolved line ratio  $\mathcal{R}_{12/13}$ ; (9) Number of bins with azimuthally stacked  $\mathcal{N}(I_{13}^{\text{stack}})$  detected with  $S/N > 4$ ; (10) Median of azimuthally stacked line ratio  $\mathcal{R}_{12/13}^{\text{stack}}$ ; (11) Far-IR flux ratio at 60 and 100 from NED ([NASA/IPAC Extragalactic Database \(NED\) 2019](#)); (12) The interacting galaxies classified in merging or post-merger stage by [Barrera-Ballesteros et al. \(2015a\)](#) are assigned to “1”, and the others are shown with “0” (13) Galaxies with bar present from HyperLEDA are indicated with number “1”, and the others are “0”.

#### 4. $^{12}\text{CO}(1-0)/^{13}\text{CO}(1-0)$ VARIATIONS

##### 4.1. Fairly Constant $\mathcal{R}_{12/13}$ Across the Sample

In Figure 3, we present the integrated global  $F_{13}$  flux, radially stacked  $I_{13}^{\text{stack}}$  and resolved  $I_{13}$  as functions of their  $^{12}\text{CO}$  counterparts.  $F_{13}$ ,  $I_{13}^{\text{stack}}$ , and  $I_{13}$  follow  $^{12}\text{CO}$  emission quite well. In the low  $I_{12}$  regime, resolved  $I_{13}$  appears 0.2-0.7 dex higher than the stacked measurements because of their limited sensitivity shown as the horizontal gray line in the left panels. In the middle panel, we repeat this line to show the  $I_{13}$  sensitivity of the individual grid, and find that the  $I_{13}^{\text{stack}}$  measurements extend well below the line. By stacking the spectra over multiple grids,  $I_{13}^{\text{stack}}$  reveals the pres-

ence of  $^{13}\text{CO}$  that is not detectable in individual grid samples.

From our integrated, stacked, and resolved  $^{13}\text{CO}$ , we measure three types of  $^{12}\text{CO}$ -to- $^{13}\text{CO}$  line ratios, all expressed in brightness temperature units: integrated line ratio  $\mathcal{R}_{12/13}^{\text{gal}} = 0.912 \times F_{12}/F_{13}$ , radial stacked ratio  $\mathcal{R}_{12/13}^{\text{stack}} \equiv I_{12}^{\text{stack}}/I_{13}^{\text{stack}}$ , and resolved line ratio  $\mathcal{R}_{12/13} = I_{12}/I_{13}$ . For the integrated line ratio, the factor 0.912 accounts for the different rest frequencies of  $^{13}\text{CO}$  and  $^{12}\text{CO}$ .  $\mathcal{R}_{12/13}^{\text{gal}}$  indicates the overall line ratio of a galaxy, comparable with the unresolved  $\mathcal{R}_{12/13}$  obtained from single-dish measurements, assuming missing flux from the interferometric observation is negligible. The values and  $1-\sigma$  uncertainties of  $\mathcal{R}_{12/13}^{\text{gal}}$  are tabulated in the fourth column of Table 1.  $^{12}\text{CO}$  missing flux of  $\sim 10$ -50% will propagate an additional  $\sim 0.5$ -10% uncertainty to the line ratio we obtain. On the other hand,

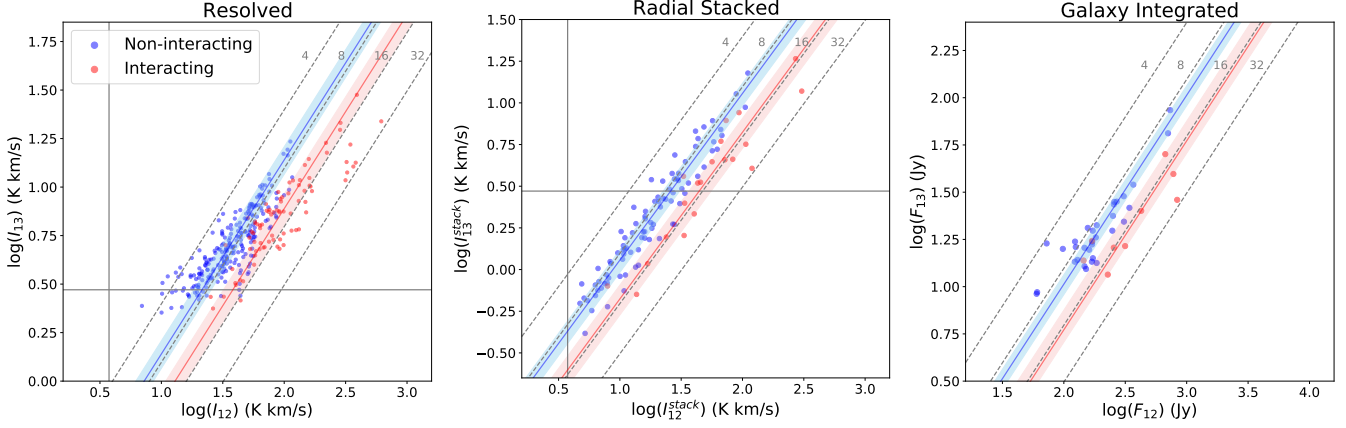


**Figure 3.**  $^{13}\text{CO}$  emissions, measured on individual grid (left panel), radial annulus, (middle) and the entire galaxy (right panel), as functions of their  $^{12}\text{CO}$  counterparts. The blue dots show the  $^{13}\text{CO}$  detections with  $S/N > 4$  in the non-interacting galaxies, while the red ones are those in the interacting galaxies. The blue and red solid lines show the median of the  $\mathcal{R}_{12/13}$  of the non-interacting and interacting galaxies, with shaded regions show the first and third quartiles of the corresponding measurements. Constant  $\mathcal{R}_{12/13}$  values of [4, 8, 16, 32] are shown as gray dotted lines in each panel. The typical detection limits of resolved  $I_{13}$  and  $I_{12}$  are shown as horizontal and vertical solid lines respectively, in the left and middle panels. Note in the middle panel, radial stacked  $I_{13}^{\text{stack}}$  approaches ranges well below this limit. All three types of measurements are closely distributed around constant values of  $\mathcal{R}_{12/13}$ .

we do not expect  $^{13}\text{CO}$  flux is lost because it is mainly originated from clumpy structures.

We provide statistics of the line ratios in Table 2. Individual line flux or intensity measurements are plotted in Figure 3, with the solid colored lines showing the median values for interacting and non-interacting galaxies and the shaded regions delineating the first and third quartiles. Remarkably, the line ratios are fairly constant among different galaxies in our sample. For the resolved  $\mathcal{R}_{12/13}$  with 323 measurements from 30 galaxies, the semi-interquartile range (SIQR) is only 2.13.

For all three types of measurements, the line ratios in the interacting galaxies are typically higher and exhibit larger scatter than those in the non-interacting galaxies. This implies the gas conditions could be systematically different due to the interaction process on large scales, therefore in the following investigations of  $\mathcal{R}_{12/13}$ , we always split our sample into interacting and non-interacting galaxies. We discuss possible mechanisms for this difference in Section 5.2.

The median line ratios increase slightly when going from resolved  $\mathcal{R}_{12/13}$  on kpc scales to global  $\mathcal{R}_{12/13}^{\text{gal}}$  on the entire galaxies. In Figure 3, resolved  $\mathcal{R}_{12/13}$  show largest scatter around a constant value indicated by the diagonal dashed lines. Stacked values  $\mathcal{R}_{12/13}^{\text{stack}}$  shift to higher values, while the integrated  $\mathcal{R}_{12/13}^{\text{gal}}$  exhibit highest values. Because the  $\mathcal{R}_{12/13}^{\text{stack}}$  measurements are mostly within  $0.4r/r_{25}$  (see Section 4.3 and Figure 5), the difference between  $\mathcal{R}_{12/13}^{\text{stack}}$  and  $\mathcal{R}_{12/13}$  is likely due to the

bias of the non-detections of  $I_{13}$  within  $0.4r/r_{25}$ , while the difference between  $\mathcal{R}_{12/13}^{\text{stack}}$  and  $\mathcal{R}_{12/13}^{\text{gal}}$  implies the non-detections beyond  $0.4r/r_{25}$  on average should have higher line ratios.

#### 4.2. Integrated $\mathcal{R}_{12/13}^{\text{gal}}$ and galaxy global properties

We carry out Spearman’s rank correlation tests between  $\mathcal{R}_{12/13}^{\text{gal}}$  and the other galaxy global properties. We first calculate Spearman’s rank correlation coefficients  $r_s$  and p-values  $P_0$  for all the 41 galaxies with  $F_{13}$  detected. Since there are likely systematic differences of the line ratio due to interaction status, we then split the sample into non-interacting and interacting galaxies, and calculate  $r_s$  and  $P_0$  respectively. The results are listed in Table 3, ordered by absolute values of  $r_s$  of all galaxies. Figure 4 shows  $\mathcal{R}_{12/13}^{\text{gal}}$  as functions of the first 12 global galaxy parameters in Table 3. Besides the 41 galaxies with  $F_{13}$  detected, for which we perform the correlation tests, we also show the lower limits on  $\mathcal{R}_{12/13}^{\text{gal}}$  with triangle symbols for the other 62 galaxies in which  $F_{12}$  is detected with  $S/N > 4$  but  $F_{13}$  is not detected; the lower limits are calculated as  $0.912F_{12}/(4\sigma(F_{13}))$ . We highlight the interacting galaxies in red in the figure; the isolated galaxies are shown in blue.

In Table 3, the absolute values  $r_s$  of non-interacting galaxies are generally smaller than that of all galaxies, and the  $P_0$  values of non-interacting galaxies are also often larger than that of all galaxies: excluding the in-

**Table 2.**  $\mathcal{R}_{12/13}$  Measurement Statistics

	All galaxies				Non-interacting galaxies				Interacting galaxies			
	$\mathcal{N}_{\text{gal}}$	$\mathcal{N}_{\text{data}}$	Median	SIQR	$\mathcal{N}_{\text{gal}}$	$\mathcal{N}_{\text{data}}$	Median	SIQR	$\mathcal{N}_{\text{gal}}$	$\mathcal{N}_{\text{data}}$	Median	SIQR
$\mathcal{R}_{12/13}$	30	323	7.97	2.13	22	241	7.24	1.20	8	82	12.92	2.44
$\mathcal{R}_{12/13}^{\text{stack}}$	41	109	9.25	2.00	32	89	8.78	1.38	9	20	15.00	3.18
$\mathcal{R}_{12/13}^{\text{gal}}$	41	41	10.21	1.74	32	32	9.70	1.19	9	9	16.92	3.18

NOTE—Number of galaxies, number of measurements, median, and semi-interquartile range (SIQR) of resolved  $\mathcal{R}_{12/13}$ , azimuthally averaged  $\mathcal{R}_{12/13}^{\text{stack}}$ , and galaxy integrated  $\mathcal{R}_{12/13}^{\text{gal}}$  in our sample.**Table 3.** Spearman’s rank correlation coefficients between global  $\mathcal{R}_{12/13}^{\text{gal}}$  and host galaxy properties

Global property	Note	Ref	All galaxies		Non-interacting galaxies		Interacting galaxies	
			$r_s$	$P_0$	$r_s$	$P_0$	$r_s$	$P_0$
$F_{12}$	$^{12}\text{CO}$ integrated flux	1	0.65	< 0.001	0.56	< 0.001	0.70	0.036
$F_{60}/F_{100}$	Far-IR flux ratio at 60 and 100 $\mu\text{m}$	2	0.53	< 0.001	0.38	0.034	0.52	0.15
$A_v$	Nebular extinction from Pipe3D	3	0.52	< 0.001	0.34	0.061	0.68	0.042
$r_{\text{mol}}/r_e$	Molecular gas concentration <sup>a</sup>	1, 3	-0.45	0.012	-0.26	0.22	-0.54	0.27
Median( $\Delta V$ )	Median velocity dispersion	4	0.41	0.01	0.21	0.25	0.36	0.39
sSFR	Specific star formation rate	3	0.35	0.025	0.30	0.1	0.40	0.29
SFR	Integrated star formation rate	3	0.28	0.078	0.33	0.074	0.27	0.49
$12 + \log(\text{O}/\text{H})$	O3N2 calibrated gas metallicity at $r_e$	3	0.15	0.36	0.14	0.44	0.77	0.072
Distance	Luminosity distance from gas line redshift	3	-0.10	0.55	-0.08	0.66	-0.20	0.61
Galaxy Type	Morphological type	5	0.06	0.71	0.25	0.16	0.88	0.0016
$M_*$	Integrated stellar mass	3	-0.05	0.77	0.01	0.95	-0.03	0.93
cos(incl)	Morph inclination	5	0.03	0.84	-0.04	0.81	-0.02	0.97

<sup>a</sup> Radius enclosing 50% of the  $^{12}\text{CO}$  flux ( $r_{\text{mol}}$ ) divided by equivalent radius ( $r_e$ )

NOTE—References: 1. Bolatto et al. (2017); 2. IRAS IR fluxes are from NED. 3. Sánchez et al. (2018); 4. Wen et al. in prep.; 5. HyperLEDA.

interacting galaxies, the correlations between  $\mathcal{R}_{12/13}^{\text{gal}}$  and global properties are weaker and less significant. We consider significant correlations with  $P_0 < 0.05$ , i.e. the significant levels of such correlations are above  $2\sigma$ . Given the sample size and uncertainty in our measurements, correlations with  $|r_s| < 0.4$  are mostly indistinguishable from random fluctuations in our data. Because the sample size of interacting galaxies are much smaller comparing to the non-interacting galaxies, their rank correlation coefficients are less reliable than the “all galaxies” and “non-interacting galaxies” samples. We proceed only discussing global correlations with  $|r_s| > 0.4$  and  $P_0 < 0.05$  for the samples of “all galaxies” and “non-interacting galaxies”, with the caution that the interacting galaxies may play important roles in some correlations found in the “all galaxies” sample.

For all the 41 galaxies with  $F_{13}$  detected, there is no strong correlation ( $|r_s| \geq 0.7$ ) between  $\mathcal{R}_{12/13}^{\text{gal}}$  and any of the the global properties we investigate in this study.  $\mathcal{R}_{12/13}^{\text{gal}}$  moderately correlates with  $F_{12}$ , infrared color  $F_{60}/F_{100}$ , median velocity dispersion, dust attenuation, and molecular gas concentration. In the non-interacting galaxies,  $\mathcal{R}_{12/13}^{\text{gal}}$  only moderately correlates with  $F_{12}$  and  $F_{60}/F_{100}$ . As shown in Figure 4, interacting galaxies tend to have higher velocity dispersion, dust attenuation and molecular gas concentration, which might account for the significantly higher  $\mathcal{R}_{12/13}^{\text{gal}}$  than the non-interacting galaxies, and lead  $\mathcal{R}_{12/13}^{\text{gal}}$  to correlate with these three parameters when they are included in the correlation tests.

The increasing  $\mathcal{R}_{12/13}$  with higher  $^{12}\text{CO}$  flux is likely due to the requirement of high  $F_{12}$  in order to detect  $F_{13}$ , which limits the  $F_{13}$ -detected galaxies to low values of  $\mathcal{R}_{12/13}^{\text{gal}}$  when  $F_{12}$  is low. Galaxies not detected in  $F_{13}$

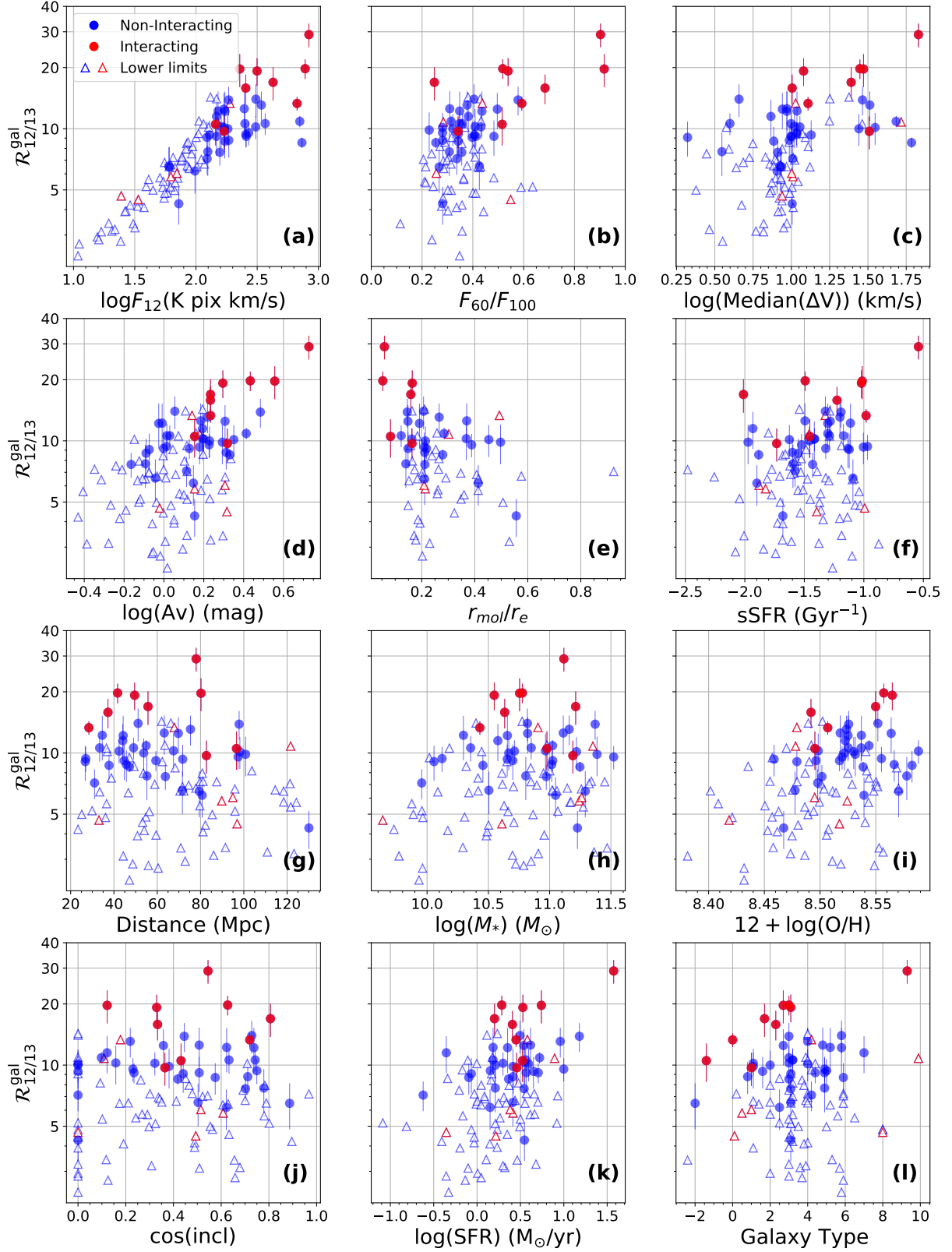


**Figure 4.** Integrated line ratio  $\mathcal{R}_{12/13}^{\text{gal}}$  as functions of global galaxy parameters for the 105 galaxies in which  $F_{12}$  is detected with  $S/N > 3$ . Blue symbols show the isolated galaxies and the red symbols show the interacting galaxies. The circles with error bars show the  $\mathcal{R}_{12/13}^{\text{gal}}$  and its uncertainty for the 41 galaxies with  $F_{13}$  detected with  $S/N > 4$ . The lower limits of  $\mathcal{R}_{12/13}^{\text{gal}}$  of the other 64 galaxies with  $F_{12}$  detected but  $F_{13}$  below the detection limits are shown as triangles. The Spearman rank correlation test results are shown in Table 3.

(shown as triangles) could potentially have higher values of  $\mathcal{R}_{12/13}^{\text{gal}}$ . The detection bias will also affect quantities that strongly correlate with  $F_{13}$ , such as  $A_V$  and possibly  $\Delta V$  (i.e. cases where the non-detections are on one side of the graph).

As shown in panel (b) of Figure 4,  $\mathcal{R}_{12/13}^{\text{gal}}$  increases with  $F_{60}/F_{100}$ ; higher  $\mathcal{R}_{12/13}^{\text{gal}}$  are associated with higher dust temperature implied by larger  $F_{60}/F_{100}$  values. This correlation is primarily driven by the starbursting galaxies which are also interacting. Such correlation still appears significant ( $P_0 < 0.01$ ) when the interacting galaxies are excluded. However, the large number of galaxies with  $F_{13}$  not detected when  $F_{60}/F_{100}$  is lower might also make the correlation ambiguous without the interacting galaxies.

#### 4.3. Radial variations in $\mathcal{R}_{12/13}$

Figure 5 summarizes the  $\mathcal{R}_{12/13}^{\text{stack}}$  radial profiles from our sample. For all the 41 galaxies with  $\mathcal{R}_{12/13}^{\text{stack}}$  detected, 7 galaxies are removed in this figure because within each of galaxies, only one bin is above the detection threshold. The radial profile of each of the 41 galaxies are shown in Appendix C). In general, interacting galaxies show systematically higher  $\mathcal{R}_{12/13}^{\text{stack}}$  at all radii than the non-interacting galaxies. For 2/3 of the non-interacting galaxies, we are able to detect the radial profiles of  $\mathcal{R}_{12/13}^{\text{stack}}$  up to  $0.4 r_{25}$  (corresponding to a galactocentric radius of typically  $\sim 6$  kpc). The remaining 1/3 are mostly barred galaxies, within which  $\mathcal{R}_{12/13}^{\text{stack}}$  are still only detected in the centers;  $\mathcal{R}_{12/13}^{\text{stack}}$  in disks of these barred galaxies below the detection limit should be higher than the detected  $\mathcal{R}_{12/13}^{\text{stack}}$  in the other non-interacting galaxies. These suggest that dynamic disturbance like interaction and bar presence could leave imprints on the radial profiles of  $\mathcal{R}_{12/13}^{\text{stack}}$ , which implies radial changes of gas conditions and/or chemical abundance.

We find a wide variety of  $\mathcal{R}_{12/13}^{\text{stack}}$  radial trends across our sample. In the galaxies without bars or interacting signatures (blue lines in Figure 5),  $\mathcal{R}_{12/13}^{\text{stack}}$  present flat or slightly increasing trends away from the galactic centers. This general trend we find is qualitatively consistent with our previous work of 11 galaxies from the CARMA STING survey (Cao et al. 2017) and a recent study of  $^{13}\text{CO}$  of 9 nearby galaxies on kpc scales by Cormier et al. (2018). Increasing  $\mathcal{R}_{12/13}$  with galactocentric radius are also reported in the Milky Way (Roman-Duval et al. 2016) and in some nearby galaxies (Meier & Turner 2004; Rosolowsky & Blitz 2005; den Brok et al. 2023). Our results are in contrast to an earlier single dish study by Paglione et al. (2001) that found  $\mathcal{R}_{12/13}$  decreases away from the galaxy center for about

half of their sample galaxies. We notice that higher  $\mathcal{R}_{12/13}^{\text{stack}}$  in the central regions or decreasing  $\mathcal{R}_{12/13}^{\text{stack}}$  radial trends are often found in barred or interacting galaxies, which may be due to large scale dynamical processes like gas flows caused by bar or interactions.

In the middle and right panels of Figure 5, we divide  $\mathcal{R}_{12/13}^{\text{stack}}$  by the each galaxy’s global line ratio  $\mathcal{R}_{12/13}^{\text{gal}}$  (listed in column (6) in Table 1) and by the  $\mathcal{R}_{12/13}^{\text{stack}}$  measured in the first radial bin. In the left panel,  $\mathcal{R}_{12/13}^{\text{stack}}/\mathcal{R}_{12/13}^{\text{gal}}$  show less scatter ( $\sim 0.2$  dex) comparing to  $\mathcal{R}_{12/13}^{\text{stack}}$  shown in Figure 5 ( $\sim 0.7$  dex) in galaxy centers within  $0.2r_{25}$ , while beyond  $0.2r_{25}$ , the scatters of  $\mathcal{R}_{12/13}^{\text{stack}}/\mathcal{R}_{12/13}^{\text{gal}}$  are similar to those of  $\mathcal{R}_{12/13}^{\text{stack}}$ . This suggests that the central variations contribute the most to galaxy-to-galaxy variations of the integrated flux ratios we measured. On the other hand, the internal variations of  $\mathcal{R}_{12/13}^{\text{stack}}$  highlighted in the right panel shows larger scatter with increasing radii; the contribution from the local variations within a galaxy become more important further away from the center. In galactic disks (with galactocentric distance  $> 0.2r_{25}$ ), the variations of  $\mathcal{R}_{12/13}^{\text{stack}}$  mixes both differences among galaxies and specific radial trends within a galaxy.

#### 4.4. $\mathcal{R}_{12/13}^{\text{stack}}$ and azimuthally averaged local properties

In this section, we investigate how  $\mathcal{R}_{12/13}^{\text{stack}}$  correlates with azimuthally averaged local properties (Section 2.5). Figure 6 summarizes the bivariate distribution of  $\mathcal{R}_{12/13}^{\text{stack}}$  and the local properties averaged azimuthally. In our sample, there are 109 measurements of  $\mathcal{R}_{12/13}^{\text{stack}}$  from 41 galaxies available. For the investigations of gas phase metallicity, star formation rate, specific star formation, and the depletion time, we exclude the annuli where less than half of the grids are identified as star forming regions. We show the non-interacting and interacting galaxies in different colors.

We calculate the Spearman’s rank correlation coefficients and list the results in Table 4. Combining all  $\mathcal{R}_{12/13}^{\text{stack}}$  from all the 41 galaxies together,  $\mathcal{R}_{12/13}^{\text{stack}}$  moderately correlates with  $I_{12}$ , specific star formation rate, and the molecular-gas-to-stellar mass fraction ( $\Sigma_{\text{mol}}/\Sigma_*$ ) with  $0.2 < |r_s| < 0.6$  and  $P_0 < 0.003$  (corresponding to  $3\text{-}\sigma$  significance). The first and to some extent the third correlations tend to be driven by the systematically higher  $^{12}\text{CO}$  in the interacting galaxies (show in the red filled circles in Figure 6). Excluding these interacting galaxies,  $\mathcal{R}_{12/13}^{\text{stack}}$  in non-interacting galaxies does not significantly correlate with  $I_{12}$ . However, the positive correlations between  $\mathcal{R}_{12/13}^{\text{stack}}$  and sSFR, as well as  $\Sigma_{\text{mol}}/\Sigma_*$ , remain significant regard-



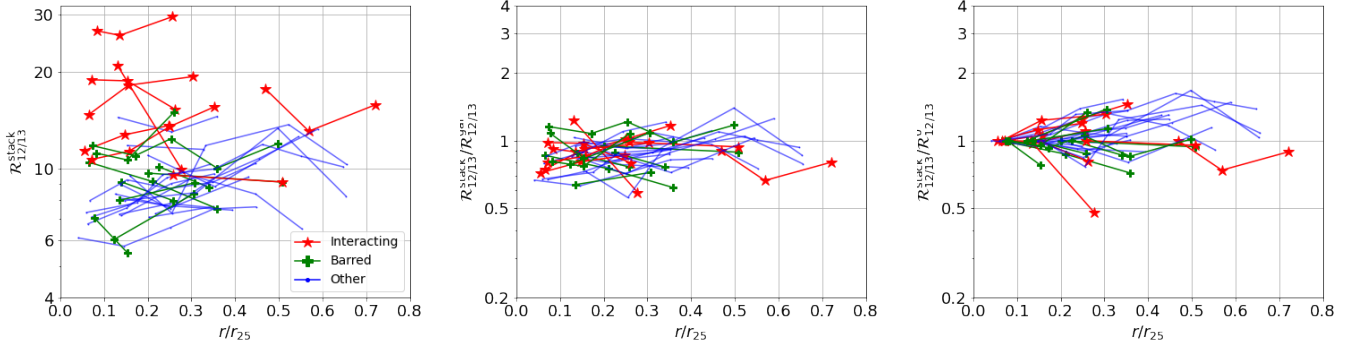


**Figure 5.** Summary of the 34 line ratio  $\mathcal{R}_{12/13}^{\text{stack}}$  radial profiles in our sample. Absolute values of  $\mathcal{R}_{12/13}^{\text{stack}}$  are shown in the left panel, the middle panel shows the  $\mathcal{R}_{12/13}^{\text{stack}}$  normalized by the each galaxy’s global line ratio  $\mathcal{R}_{12/13}^{\text{gal}}$ , and the right panel shows  $\mathcal{R}_{12/13}^{\text{stack}}$  divided by  $\mathcal{R}_{12/13}^{\text{stack}}$  at the central radial bin ( $\mathcal{R}_{12/13}^0$ ). Interacting galaxies are shown in red star symbols, and barred, non-interacting galaxies are shown in green crosses. The other unbarred, non-interacting galaxies are shown in blue lines. Within an non-interacting, unbarred galaxy,  $\mathcal{R}_{12/13}^{\text{stack}}$  are fairly constant as a function of radius, with possible tendency of slight increase beyond  $0.2\text{--}0.3r_{25}$ ; outliers from the general trend are exclusively found in barred or interacting galaxies.

**Table 4.** Spearman’s rank correlation coefficients between  $\mathcal{R}_{12/13}^{\text{stack}}$  and azimuthally averaged local parameters

Parameter	Note	Ref	All galaxies		Non-interacting galaxies		Interacting galaxies	
			$r_s$	$P_0$	$r_s$	$P_0$	$r_s$	$P_0$
$I_{12}^{\text{stack}}$	Stacked $^{12}\text{CO}$ intensity	1,2	0.32	< 0.001	0.11	0.32	0.23	0.33
$I_{13}^{\text{stack}}$	Stacked $^{13}\text{CO}$ intensity	2	0.00	0.97	−0.18	0.095	−0.11	0.64
$\sigma_{12}^{\text{stack}}$	Stacked $^{12}\text{CO}$ line width	1,2	−0.00	0.98	−0.15	0.16	0.06	0.82
$\Sigma_*$	Mean stellar mass surface density	3	−0.04	0.65	−0.20	0.06	0.01	0.96
$Z_{\text{mwt}}$	Mean mass weighted stellar metallicity	3	−0.17	0.074	−0.17	0.11	−0.08	0.74
$\text{Age}_{\text{mwt}}$	Mean mass weighted stellar age	3	−0.11	0.23	−0.16	0.13	−0.13	0.57
$A_V$	Mean nebular extinction from Pipe3D	3	0.12	0.22	0.05	0.61	−0.04	0.87
$12 + \log(\text{O}/\text{H})$	Median gas phase metallicity from O3N2	3	0.01	0.9	0.09	0.41	0.37	0.17
$\Sigma_{\text{SFR}}$	Mean star formation rate surface density	3	0.17	0.086	0.04	0.69	−0.02	0.94
$s\text{SFR}$	Mean specific star formation rate	3	0.36	< 0.001	0.32	0.0026	0.25	0.37
$\Sigma_{\text{mol}}/\Sigma_*$	Mean molecular gas to stellar mass fraction	2	0.56	< 0.001	0.43	< 0.001	0.43	0.057
$t_{\text{dep}}$	Mean depletion time assuming constant $X_{12\text{CO}}$	2	−0.04	0.7	−0.07	0.55	0.01	0.96

NOTE— All these local properties are averaged azimuthally. References: 1. Bolatto et al. (2017); 2. This work; 3. Sánchez et al. (2016b).

less whether or not we exclude the interacting galaxies. In interacting galaxies, there are no significant correlations above  $2\sigma$  significance.

Except for these four parameters,  $I_{12}$ ,  $s\text{SFR}$ , and  $\Sigma_{\text{mol}}/\Sigma_*$ , we do not find any other significant trends of  $\mathcal{R}_{12/13}^{\text{stack}}$  with the local properties averaged on each annulus. A positive trend between  $\mathcal{R}_{12/13}$  and SFR has been reported before by Davis (2014) using galaxy-integrated measurements, while our  $\mathcal{R}_{12/13}^{\text{stack}}$  measurements suggest no correlation with SFR. Neither the interacting nor non-interacting sample has a  $P_0$  supporting a significant correlation with SFR.

For each of the correlations we investigate, we perturb the  $\mathcal{R}_{12/13}^{\text{stack}}$  values by its measurement uncertainties 1000

times to obtain the  $r_s$  and  $P_0$  values distributions. We characterise the uncertainties of  $r_s$  and  $P_0$  by their SIQR from these distributions. Our conclusions on the significance of each correlation remain the same when taking the  $r_s$  and  $P_0$  uncertainty into consideration.

Note that with the spectral stacking technique, we are able to measure  $\mathcal{R}_{12/13}^{\text{stack}}$  values from  $I_{13}^{\text{stack}}$  that are well below the limit that the individual  $I_{13}$  detection threshold imposes (the horizontal gray lines in Figure 3). Such detection threshold on  $I_{13}$  could introduce a strong positive trend of  $\mathcal{R}_{12/13}$  with increasing  $I_{12}$ , which is due to the biased  $I_{13}$  detections towards lower  $I_{12}$  end (as the horizontal lines in Figure 3 intersect with lower values of  $\mathcal{R}_{12/13}$  shown in dotted lines; see Appendix 4.4 for

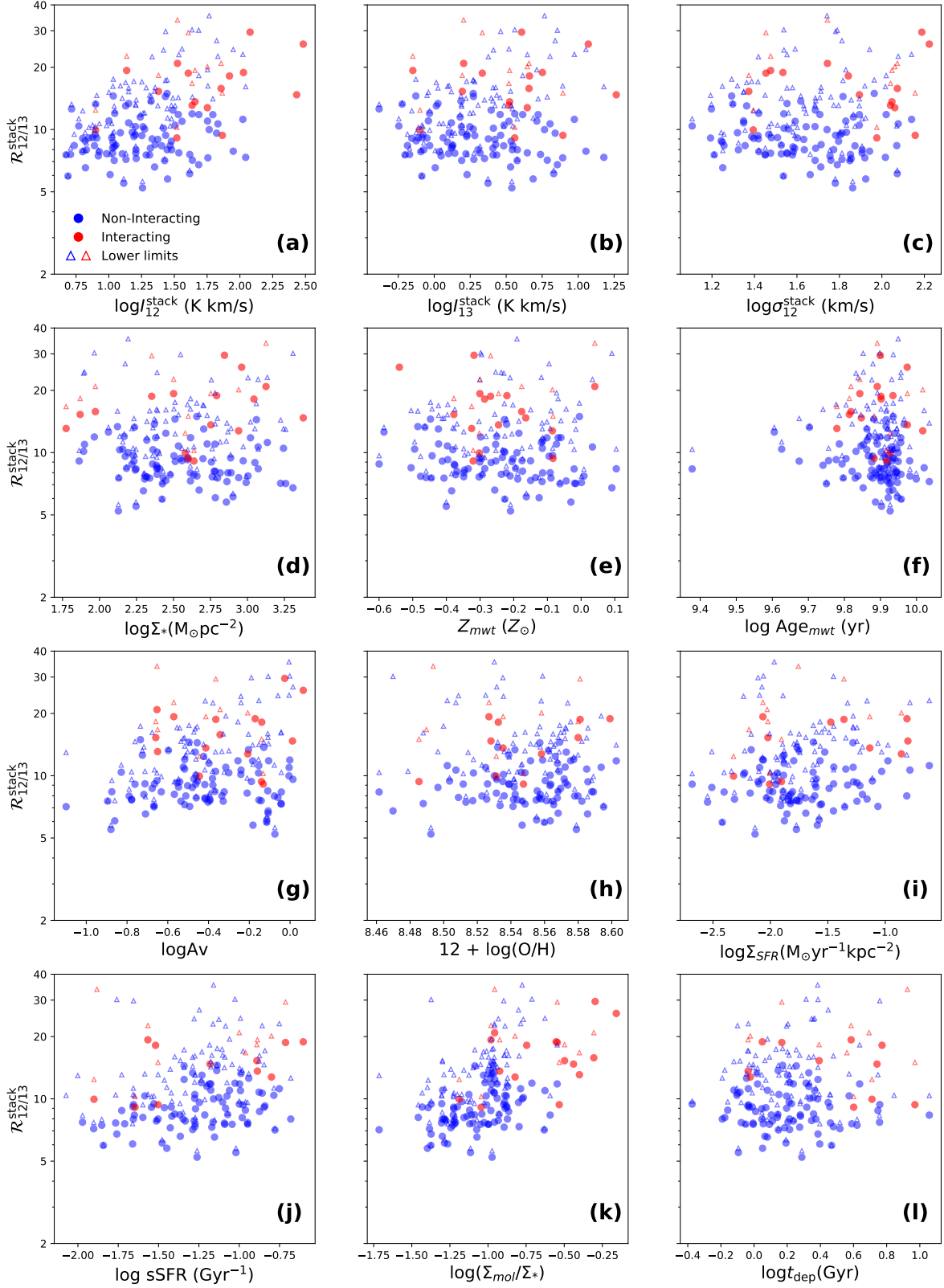


**Figure 6.** Radial-stacked line ratio  $\mathcal{R}_{12/13}^{\text{stack}}$  as functions of azimuthally averaged properties in the 41 galaxies with radial stacked  $^{13}\text{CO}$  detected with  $\text{S/N} > 4$  from our sample. The explanations of x-axis labels and the Spearman rank correlation test results are shown in Table 4. In panels (h), (i), (j), (l), we exclude the radius bin if it contains less than 50% grids identified as star forming regions with the BPT diagnostics. The filled circles show the individual azimuthally averaged  $\mathcal{R}_{12/13}^{\text{stack}}$  measurements for annuli with stacked  $^{13}\text{CO}$  detected with  $\text{S/N} > 4$  in the non-interacting (blue) and interacting (red) galaxies. The lower limits of  $\mathcal{R}_{12/13}^{\text{stack}}$  for annuli with stacked  $^{13}\text{CO}$  undetected are shown in triangles.

more details about this bias effect on resolved measurements). Our  $\mathcal{R}_{12/13}^{\text{stack}}$  show no correlation with  $I_{12}$  for non-interacting galaxies; the detection bias is eliminated at some extent by stacking multiple spectra together. However, we should be cautious that these  $\mathcal{R}_{12/13}^{\text{stack}}$  detections are still biased: in the EDGE-CALIFA survey, there are remaining 63 galaxies that we only detect  $I_{12}^{\text{stack}}$  but not  $I_{13}^{\text{stack}}$  (or  $\mathcal{R}_{12/13}^{\text{stack}}$ ).

## 5. DISCUSSION

Using kpc scale CO interferometric observations in 105 nearby galaxies from the EDGE-CALIFA survey, we measure the  $^{12}\text{CO}$  to  $^{13}\text{CO}$  line ratio  $\mathcal{R}_{12/13}$  from kpc scales to entire galaxies, and investigate how they correlate with global galaxy properties (Section 4.2), galactocentric distance (Section 4.3), and other resolved properties (Section 4.4). Here we briefly describe the mechanisms that cause  $\mathcal{R}_{12/13}$  variations first. We then summarize our results to identify the parameters that are related the observed  $\mathcal{R}_{12/13}$  on kpc scales and the possible mechanisms of these relations.

### 5.1. Possible causes of $\mathcal{R}_{12/13}$ variations

Causes of variations in  $\mathcal{R}_{12/13}$  can be grouped into the following three broad categories.

*Abundance variations*—Changes in the isotopic abundance ratio ( $[^{12}\text{C}/^{13}\text{C}]$ ) can directly impact  $\mathcal{R}_{12/13}$  if variations in optical depth are of secondary importance. In the Milky Way, a positive gradient with Galactocentric distance has been observed in the isotopic abundance ratio (Milam et al. 2005), which may contribute to a positive observed gradient in  $\mathcal{R}_{12/13}$  (Roman-Duval et al. 2016). The radial  $[^{12}\text{C}/^{13}\text{C}]$  gradient may reflect stellar population differences since  $^{12}\text{C}$  production skews toward massive stars while  $^{13}\text{C}$  production skews toward intermediate-mass stars. In general, however,  $[^{12}\text{C}/^{13}\text{C}]$  is difficult to measure because of the much higher opacity of  $^{12}\text{C}$ -bearing species. Furthermore, the *isotopologue* abundance ratio  $[^{12}\text{CO}/^{13}\text{CO}]$  may depart from the isotopic ratio in the presence of chemical fractionation (which favors  $^{13}\text{CO}$  production in cold regions, Watson et al. 1976) or selective photodissociation (which tends to destroy  $^{13}\text{CO}$  in unshielded regions, Bally & Langer 1982). The abundance ratio of optically thinner isotopologues, e.g.  $[^{13}\text{CO}/\text{C}^{18}\text{O}]$ , can provide a more unambiguous diagnostic (e.g. Jiménez-Donaire et al. 2017), although it also involves the  $[^{16}\text{O}/^{18}\text{O}]$  ratio. Abnormally low  $^{13}\text{CO}/\text{C}^{18}\text{O}$  intensity ratios in ULIRGs, for instance (e.g. Sliwa et al. 2017; Brown & Wilson 2019), appear inconsistent with chemical fractionation or selective photodissociation, and support the hypothesis that the high  $\mathcal{R}_{12/13}$  in these galaxies is due to recent ISM

enrichment by massive stars (see also Viti et al. 2020, for theoretical evidence).

*Opacity changes in LTE*—A simple prediction based on the assumptions of LTE and fixed  $^{12}\text{CO}$  and  $^{13}\text{CO}$  abundances is that

$$\mathcal{R}_{12/13} \propto \frac{1}{\tau(^{13}\text{CO})} = \left[ \frac{^{12}\text{CO}}{^{13}\text{CO}} \right] \frac{1}{\tau(^{12}\text{CO})} \propto \frac{T_k^2 \Delta v}{N_{\text{H}_2}}, \quad (5)$$

for optically thick  $^{12}\text{CO}$  and optically thin  $^{13}\text{CO}$  (e.g., Paglione et al. 2001). Thus, opacity variations that stem from changes in molecular gas column density, temperature, and/or line widths could lead to variations in  $\mathcal{R}_{12/13}$ . Specifically,  $\mathcal{R}_{12/13}$  should increase with increasing temperature or line width and decrease with increasing column density. Previous studies have suggested that line broadening due to the stellar feedback may contribute to the increasing trend of  $\mathcal{R}_{12/13}$  with SFR (Crocker et al. 2012; Davis 2014). A recent study using a sample of 80 galaxies observed by 45 m Nobeyama telescope find that  $\mathcal{R}_{12/13}$  increases with sSFR (Morokuma-Matsui et al. 2020). Even without significant feedback, line broadening may result from the higher velocity dispersion needed to support the gas disk in denser regions of galaxies (Aalto et al. 1995). However, no significant correlation between  $\mathcal{R}_{12/13}$  and line width or SFR surface density has been found in several kpc-scale studies within individual galaxies (Meier & Turner 2004; Cao et al. 2017; Cormier et al. 2018). These discrepant results may arise from higher gas column density  $N_{\text{H}_2}$  compensating for the higher  $T_k$  and  $\Delta v$  in regions of high SFR.

*Non-LTE Effects*—An LTE interpretation of  $\mathcal{R}_{12/13}$  implicitly assumes that the density is high enough to thermalize both lines, and that both lines originate from the same volume and thus experience the same degree of beam dilution. However, if the volume density is low,  $\mathcal{R}_{12/13}$  will increase since  $^{13}\text{CO}$  is mostly sub-thermally excited while  $^{12}\text{CO}$ , with a lower effective critical density, remains bright. The presence of such low-density gas can strongly influence the observed line ratios if it fills a larger volume than the denser  $^{13}\text{CO}$ -emitting gas. The model based on non-LTE radiative transfer and a log-normal volume density distribution within a beam developed by Leroy et al. (2017) demonstrates that for fixed opacity, temperature, and abundance, the differential excitation roughly accounts for 0.2 dex variations of  $\mathcal{R}_{12/13}$  below a mean density of  $10^3 \text{ cm}^{-3}$ . Above  $10^3 \text{ cm}^{-3}$ , this effect is quite negligible.

In the non-LTE regime, the positive correlation between temperature and  $\mathcal{R}_{12/13}$  may be substantially reduced or even reversed compared to the LTE case (e.g.,

Hirota et al. 2010). Roughly speaking, this is because the higher temperature causes the peak emissivity of both lines to shift to lower densities, allowing  $^{13}\text{CO}$  to emit more efficiently and reducing  $\mathcal{R}_{12/13}$ . Assuming molecular emission lines emerging from a log-normal distribution of densities at a mean density of  $400 \text{ cm}^{-3}$  (i.e.  $10^{2.6} \text{ cm}^{-3}$ ) and an initial temperature of 15 K, the non-LTE radiative transfer modeling shows that an increase of the temperature by a factor of 2 leads to a decrease of  $\mathcal{R}_{12/13}$  by roughly the same factor (Puschign 2020).

### 5.2. Elevated $\mathcal{R}_{12/13}$ in interacting galaxies

In our sample, we find the most striking factor that affects the  $\mathcal{R}_{12/13}$  values in a galaxy is whether or not it is experiencing a strong interaction.  $\mathcal{R}_{12/13}$  in interacting galaxies tends to be systematically higher than non-interacting galaxies from kpc scale to the entire galaxy (Figure 3). The  $\mathcal{R}_{12/13}^{\text{stack}}$  radial profiles of interacting galaxies show a similar enhancement (Figure 5). Moreover, we can infer from Figures 6 and 11 that these differences between interacting and non-interacting galaxies are unlikely due to their differences in other resolved properties except for  $I_{12}$  and  $A_v$ , since both of interacting and non-interacting samples share the similar parameter spaces. This similarity suggests that independently from other local parameters, the gas conditions are systematically different due to the interaction process on large scales.

Higher global  $\mathcal{R}_{12/13}^{\text{gal}}$  values in merging galaxies, especially (U)LIRGs have been reported by single dish surveys reported than in normal spiral galaxies (e.g. Aalto et al. 1991; Casoli et al. 1991, 1992). The observed resolved  $\mathcal{R}_{12/13}$  of merging galaxies on smaller scales from different individual studies also tend to be higher than the typical  $\mathcal{R}_{12/13}$  observed in normal galaxies (e.g. Young & Scoville 1984; Taniguchi & Ohyama 1998; Henkel et al. 2014; Aalto et al. 2010). In our previous systematic study of resolved  $\mathcal{R}_{12/13}$  from the STING survey, the highest  $\mathcal{R}_{12/13}$  is found in the interacting galaxy NGC 5713 (Cao et al. 2017). Our results from the CARMA EDGE survey confirm that this.

During the interaction process, the gas is driven toward the inner few kpc of the galaxy and triggers active star formation. Both the stars and interstellar medium are strongly perturbed during the process. For example, the molecular clouds could be disrupted to diffuse gas due to the dynamical disturbance. The physical conditions in molecular gas during the merging process are expected to be different from the gas in normal, non-interacting galaxies.

We notice that the systematically higher  $\mathcal{R}_{12/13}$  is due to enhanced  $I_{12}$  emission rather than reduced  $I_{13}$  in the

interacting galaxies (Figures 3 and 6 panels (a) and (b)), confirming the same finding by Casoli et al. (1992) but down to the kpc scales. With the similar  $I_{13}$ , we would expect that the  $^{13}\text{CO}$  column density in the interacting galaxies is also similar to that in the non-interacting galaxies. Assuming  $^{13}\text{C}$  or  $^{13}\text{CO}$  abundance in the interacting galaxies remain the same, the elevated  $\mathcal{R}_{12/13}$  and enhanced  $^{12}\text{CO}$  is mainly due to the reduced opacity of  $^{12}\text{CO}$  emission. Under the LTE assumption, higher temperature and/or broader line width would reduce the  $^{12}\text{CO}$  opacity.

Unfortunately, we do not have the direct temperature or the velocity dispersion measured for the molecular gas. We can only infer these effects from indirect parameters. On the galaxy scale, we show that higher  $\mathcal{R}_{12/13}^{\text{gal}}$  are associated with highest IR colors in the interacting galaxies in panel (b) of Figure 4, suggesting that temperature could be part of the reason. Meanwhile, two of the interacting galaxies with very low IR colors (NGC5614 and UGC08107) still show higher  $\mathcal{R}_{12/13}^{\text{gal}}$ , implying that the temperature cannot be the only mechanism that account for the higher  $\mathcal{R}_{12/13}^{\text{gal}}$  in interacting galaxies. On the other hand, in panel (c) of Figure 4  $\mathcal{R}_{12/13}^{\text{gal}}$  we find that the typical (median) velocity dispersion in the interacting galaxies tend to be higher than the non-interacting galaxies; elevated  $\mathcal{R}_{12/13}$  in interacting galaxies might be explained by the broadened line width in them.

If it is the higher temperature and/or broader line width that reduce the  $^{12}\text{CO}$  opacity and thus elevate the  $\mathcal{R}_{12/13}$  in the interacting galaxies, we should also see similar effects on kpc scales. However, such effects are not prominent on kpc scales: except for Arp 220, the line widths of the azimuthally stacked  $^{12}\text{CO}$  in interacting galaxies are not significantly higher than that in the non-interacting galaxies (panel (c) of Figure 6). In addition, both the line width and gas temperature are expected to increase with star formation, but we do find that SFR surface density in interacting galaxies is higher than the others (panel (i) of Figure 6). The apparent discrepancy on galaxy and kpc scales implies that the non-LTE effects and/or abundance anomaly are more likely the reasons for the systematic difference in  $\mathcal{R}_{12/13}$  in the interacting galaxies.

One explanation to our observed higher  $\mathcal{R}_{12/13}$  in interacting galaxy on all scales is that the large-scale gas inflows induced by the interactions make the non-LTE effects or abundance changes prominent in these systems, especially in the centers. In non-interacting galaxies, we find that radial profiles of  $\mathcal{R}_{12/13}$  generally show increasing trends (Figure 5), which are likely caused by the less dense or less processed gas at larger radii. Dur-

ing the interacting process,  $\mathcal{R}_{12/13}$  could be elevated by the inflow of gas from outer regions with higher  $\mathcal{R}_{12/13}$ . The inflow might last for a period of time, funnelling the gas to centers and enhancing the molecular gas concentration gradually. Indeed, we see a wide spread of gas concentrations in the interacting galaxies (Figure 4 panel (e)), with three of them show the highest gas concentrations in our sample. As the interaction proceeds, the gas inflow should not stay in low density but form denser gas or more molecular clouds, and thus triggers more star formation in the center. The increased fraction of denser gas in later times is plausible, as the strongest  $^{13}\text{CO}$  emission which likely traces denser gas are found in the advanced mergers like Arp 220, NGC 2623, and NGC 5218. It is also in the galaxies that we find the enhanced SFR; the triggered starburst can then in turn increase  $\mathcal{R}_{12/13}$  via opacity effects. In fact, the two late stage mergers (Arp 220 and NGC 2623) also have the highest IR color and median velocity dispersion, which may further enhance their  $\mathcal{R}_{12/13}$  values.

The gas inflow could also induce lower abundance ratio of  $^{12}\text{C}/^{13}\text{C}$ . The metal-poor gas from the outer regions dilute the metallicity in interacting galaxies (e.g. Kewley et al. 2000). In particular, this dilution is observed on large scales (Barrera-Ballesteros et al. 2015b), as the star formation triggered in centers could enrich the ionized gas abundance there. However, in our case of  $^{12}\text{C}/^{13}\text{C}$ , both the inflow of less processed gas and recent massive star formation could drive it to higher values, which may raise  $\mathcal{R}_{12/13}$  both locally and on large scale.

Building a matched control sample to compare the interacting and non-interacting galaxies in details is beyond the scope of this paper. Nevertheless, our data suggests that the  $\mathcal{R}_{12/13}$  in interacting systems tends to be higher than non-interacting galaxies, implying the physical conditions in the molecular gas or its chemical abundance are changed by the interacting process. Due to the limited sample, we also do not study impact of detailed stages of interactions. Since interacting processes are complex and there are many different types of interacting galaxies and mergers, future multi-line observations including  $^{13}\text{CO}$  for a representative sample of interacting galaxies would be helpful to unravel more details about interactions.

### 5.3. A complex picture of $\mathcal{R}_{12/13}$ on kpc scales

$\mathcal{R}_{12/13}$  measured on kpc scales and across the entire galaxy are fairly constant among our sample. Although bearing some detection bias, this is still remarkable considering our sample's diversity. However, this does not mean that the gas conditions remain constant. The lack of strong variations in  $\mathcal{R}_{12/13}$  reveals a complex picture

of observed  $\mathcal{R}_{12/13}$  in galaxies. The variations in  $\mathcal{R}_{12/13}$  cannot be attributed to a single factor; instead, several different mechanisms determines  $\mathcal{R}_{12/13}$  from kpc to the entire galaxies.

We discuss in Section 5.2 that  $\mathcal{R}_{12/13}$  in interacting galaxies is likely elevated due to the merging process. For the remaining non-interacting galaxies,  $\mathcal{R}_{12/13}$  slightly increases with the IR color  $F_{60}/F_{100}$  (panel B in Figure 4). The higher dust temperature is expected to be associated with active star formation, so these results are consistent with previous galaxy surveys (Davis 2014; Morokuma-Matsui et al. 2020). However, we do not find that  $\mathcal{R}_{12/13}^{\text{gal}}$  correlates with the characteristic SFR or sSFR measured at effective radius (panels (k) and (f) in Figure 4). We also do not find that  $\mathcal{R}_{12/13}$  correlates with SFR or sSFR surface densities measured on kpc scale annulus (Figure 6), which generally agrees with the previous kpc scale studies (Cao et al. 2017; Cormier et al. 2018). The apparent discrepancy between our global and resolved results suggest that the temperature may cause the galaxy-to-galaxy variations in  $\mathcal{R}_{12/13}$ , but the variations within a galaxy due to other effects might wash it out when we combine all the resolved  $\mathcal{R}_{12/13}$  measurements.

The  $\mathcal{R}_{12/13}^{\text{stack}}$  measured on annuli suggest that the  $\mathcal{R}_{12/13}^{\text{stack}}$  variations in galaxy centers are likely contribute most to the galaxy-to-galaxy differences (Figure 5). We perform the correlation tests for  $\mathcal{R}_{12/13}^{\text{stack}}$  and other local properties following the same methods as in Section 4.4, restricting the measurements to be within  $0.2r_{25}$  instead of using all the detected values. We find that in the galaxy center,  $\mathcal{R}_{12/13}^{\text{stack}}$  increase with the azimuthally averaged SFR and sSFR surface density (Figure 7). For the SFR, the general trend roughly follows the empirical fitting from Davis (2014). The correlation between  $\mathcal{R}_{12/13}^{\text{stack}}$  and sSFR in our sample is weaker and less significant than Morokuma-Matsui et al. (2020), shown as the dotted line in the right panel of Figure 7. Note our  $\mathcal{R}_{12/13}^{\text{stack}}$  over the central two annuli are typically lower than their  $\mathcal{R}_{12/13}$  stacked over the entire galaxy by 10%. These trends found in galaxy centers is generally consistent with the integrated correlations in both our and other studies (e.g. Young & Sanders 1986b; Sage & Isbell 1991; Aalto et al. 1991, 1995; Crocker et al. 2012; Davis 2014; Vila-Vilaro et al. 2015; Herrero-Illana et al. 2019; Morokuma-Matsui et al. 2020), where  $\mathcal{R}_{12/13}^{\text{gal}}$ , IR color, SFR, and sSFR measured integrat- edly all have large contributions from the galaxy centers. On the other hand, we do not find  $\mathcal{R}_{12/13}^{\text{stack}}$  significantly correlate with SFR or sSFR in other radius bins beyond  $0.2r_{25}$ . Therefore, it seems that that  $\mathcal{R}_{12/13}$  increases with stellar feedback, either through the reduced

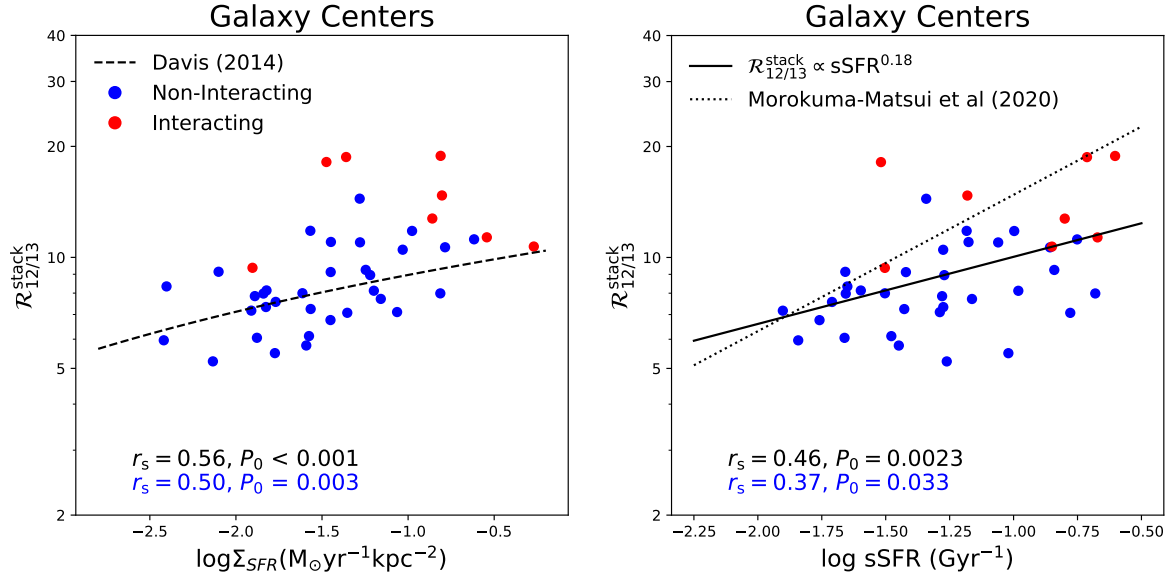


**Figure 7.** Stacked line ratio  $\mathcal{R}_{12/13}^{\text{stack}}$  vs. azimuthally averaged SFR (left) and sSFR (right) surface density in galaxy centers (within  $0.2r_{25}$ ). The labels and colors are the same as in Figure 6. In the left panel, the dashed line shows empirical relation derived by Davis (2014). In the right panel, the solid line is the fitting based our sample, and the dotted line shows the fitting by Morokuma-Matsui et al (2020). The Spearman rank coefficients are shown in black and blue color in the bottom for all the galaxies and for non-interacting galaxies respectively.

opacity due to higher temperature and/or velocity dispersion, but these effects are likely only prominent in galaxy centers. Higher  $^{12}\text{CO}/^{13}\text{CO}$  abundance might also play a role there, as multi-line modeling suggests higher  $^{12}\text{CO}/^{13}\text{CO}$  associated with higher star formation activities (e.g. Topal 2020). However, in galaxy disks, the variations of  $\mathcal{R}_{12/13}$  seem more complex that non-LTE effects must be taken into account.

Within a non-interacting galaxy,  $\mathcal{R}_{12/13}^{\text{stack}}$  in general slightly increases with radius (Figure 5). For massive main-sequence galaxies, the sSFR also generally increases with radius. Indeed, we find that for the non-interacting galaxies without bars, within a galaxy, both sSFR and  $\mathcal{R}_{12/13}^{\text{stack}}$  show increasing trend, implying a positive correlation between them. This correlation is more likely due to the non-LTE effects, otherwise we would also see a correlation between  $\mathcal{R}_{12/13}^{\text{stack}}$  and SFR or sSFR across different galaxies. As sSFR increases with radius as the volume density decreases, a substantial fraction of  $^{13}\text{CO}$  might be subthermally excited and thus  $\mathcal{R}_{12/13}$  increases. Indeed, our detections of resolved  $^{13}\text{CO}$  drastically drops with increasing galactocentric distances (Figure 1). Meanwhile, the increasing sSFR reflects the inside-out growth of a galaxy, from which we also expect positive radial  $^{12}\text{C}/^{13}\text{C}$  abundance gradient. Such abundance gradient could also explain the slightly increasing trend of  $\mathcal{R}_{12/13}$  with sSFR and galactocentric radii within a galaxy.

We also find  $\mathcal{R}_{12/13}^{\text{stack}}$  increases with increasing molecular gas fraction (Figure 6 panel(k)). Since we calculate the molecular gas using fixed  $X$  factor based on  $^{12}\text{CO}$  emission, this means what we find is essentially a positive correlation between  $^{13}\text{CO}$  emission and underlying stellar surface density. The increased  $^{13}\text{CO}$  with increasing stellar surface density seems to reflect the higher averaged density of gas due to the gravity fields. However, the lack of (anti-)correlation between  $\mathcal{R}_{12/13}^{\text{stack}}$  and stellar surface density (Figure 6 panel (d)) emphasizes that the gas density cannot be a dominating driver of  $\mathcal{R}_{12/13}$  variations. For example, stellar feedback from new stars forming with denser gas can reduce the  $^{12}\text{CO}$  opacity and increase  $\mathcal{R}_{12/13}$ .

In summary, our study reveals a complex picture of observed  $\mathcal{R}_{12/13}$  on kpc scale in galaxies. Variations in  $\mathcal{R}_{12/13}$  on kpc scales are not very sensitive to any particular local environments or the global galaxy properties in general; there seems to be no single driver of the  $\mathcal{R}_{12/13}$  variations. In our sample, the weak correlations we find suggest stellar feedback could increase  $\mathcal{R}_{12/13}$  in galaxy centers. In galaxy disks, non-LTE effects and/or abundance variations become important in determining  $\mathcal{R}_{12/13}$ . Moreover, dynamical disturbance like interacting process or bar presence could result in  $\mathcal{R}_{12/13}$  that deviate from the other galaxies.

#### 5.4. Caveats of this study

One caveat of this study is that we do not have single dish observations for the calculations of the line ratios. There could be  $^{12}\text{CO}$  emissions that are missed in our interferometric observations: extended emission might be filtered out by the lack of short spacings, and weak  $I_{12}$  on smaller scales are missed due to the relatively low brightness sensitivity of interferometers compared to single dishes. The effect of spatial filtering on the intensity and  $\mathcal{R}_{12/13}$  measurement of each galaxy is unclear, but are more likely to affect  $^{12}\text{CO}$  than  $^{13}\text{CO}$ . Although we do not see indications that EDGE misses a large fraction of the  $^{12}\text{CO}$  flux (Bolatto et al. 2017), observing the sample galaxies in single dish telescopes such as IRAM and GBT will improve the absolute line ratio values measured in this study.

When searching for correlations between  $\mathcal{R}_{12/13}$  and local properties, to reduce the detection bias due to the limited sensitivity of  $^{13}\text{CO}$  on resolved kpc scales, we use the azimuthal stacked spectra and the averaged local properties. This inevitably removes signatures of azimuthal variations of  $\mathcal{R}_{12/13}$ . Higher sensitivity  $^{13}\text{CO}$  observations on kpc-scales over a representative sample are required to fill the gap between cloud-scale studies and the galaxy evolution.

In this study, we focus on  $^{13}\text{CO}$  and its comparison to  $^{12}\text{CO}$ . We use their line ratio  $\mathcal{R}_{12/13}$  to infer the underlying variations of gas conditions. However, the mechanisms that determines  $\mathcal{R}_{12/13}$  are complex, which makes it impossible to infer the gas conditions under the simplest LTE assumptions. For non-LTE radiative transfer modeling to provide improved constraints on gas properties, additional high-J CO lines are strongly desired.

Last but not least, we still do not have good understanding of the  $^{13}\text{C}$  or  $^{13}\text{CO}$  abundance in other galaxies. There are only a few direct measurements  $^{13}\text{C}$  (e.g. Henkel et al. 2014; Tang et al. 2019). Even with the multi-line diagnostics, this will still be a problem that could introduce large uncertainties on gas conditions constraints. Future observations on  $^{13}\text{C}$  abundance will be desired to better interpret the  $^{13}\text{CO}$  observations and improve the multi-line modeling in extragalactic studies.

## 6. CONCLUSIONS

We present  $^{13}\text{CO}$  observations for the EDGE-CALIFA survey, which is a mapping survey of 126 nearby galaxies at a typical spatial resolution of 1.5 kpc. We measure the  $^{12}\text{CO}$ -to- $^{13}\text{CO}$  line ratio  $\mathcal{R}_{12/13}$  resolved on kpc scales, averaged in annuli, and integrated over the entire galaxies. Combining our  $^{13}\text{CO}$  and  $^{12}\text{CO}$  observations with optical spectroscopy IFU data from the CALIFA survey, we perform a systematic study of  $\mathcal{R}_{12/13}$  in relation to

with local environments and their host galaxy properties for a wide variety of galaxies. Since  $\mathcal{R}_{12/13}$  variations could reflect the changes of physical conditions or chemical abundance of molecular gas, such a systematic study on  $\mathcal{R}_{12/13}$  provides useful implications for understanding the physics of molecular ISM and star formation in the context of galaxy evolution. Our main conclusions are as follows:

1. We detect resolved  $^{13}\text{CO}$  in 30 galaxies from the 126 galaxies in the EDGE-CALIFA survey. By stacking the spectra in annuli and integrating over regions detected in  $^{12}\text{CO}$ , we also measure azimuthally averaged and integrated  $^{13}\text{CO}$ . The  $^{13}\text{CO}$  emission measured on different scales closely associates the the strength of the  $^{12}\text{CO}$  emission (Figure 3).  $\mathcal{R}_{12/13}$  in our sample distribute in a narrow range, with median of 7.97 and semi-interquartile range (SIQR) of 2.13 (Table 2).
2. We find that the global, the azimuthally averaged, and the resolved line ratios  $\mathcal{R}_{12/13}$  in interacting galaxies are systematically higher than in the non-interacting galaxies. Thus the interaction process seems to enhance the  $^{12}\text{CO}$  emission from entire galaxies down to kpc scales. Inflow of less dense and less processed gas with higher  $[^{12}\text{C}/^{13}\text{C}]$  from large radii during the interacting process is a possible mechanism to drive the higher  $^{12}\text{CO}$  and  $\mathcal{R}_{12/13}$  on all scales.
3. We present annulus-averaged  $\mathcal{R}_{12/13}$  radial profiles for our sample, taking into account the  $^{13}\text{CO}$  non-detections by spectral stacking (Figure 10). We find that roughly half of galaxies show increased  $\mathcal{R}_{12/13}$  beyond  $0.2R_{25}$ , suggesting more optically thin gas or lower  $^{13}\text{C}$  abundance in the disks relative to the centers in general. Decreasing radial trends of  $\mathcal{R}_{12/13}^{\text{stack}}$  are mostly seen in interacting galaxies or barred galaxies, which may reflect the less dense or processed gas inflows from large radii due to large scale dynamic processes.
4. We study  $\mathcal{R}_{12/13}$  in relation to the stellar population and other ISM components within galaxies and to the global parameters of the galaxies. We do not find strong correlation between  $\mathcal{R}_{12/13}$  and any local or global properties we investigate (Figure 4). In particular for non-interacting galaxies, while increased global  $\mathcal{R}_{12/13}^{\text{gal}}$  with increasing IR color hints at reduced opacity due to higher temperature, we do not find the azimuthally averaged  $\mathcal{R}_{12/13}^{\text{stack}}$  to be significantly correlated with local SFR (Figure 6). The lack of uni-

versal and strong correlations on different scales reveals a complex picture of molecular structure and the importance of multi-scale processes of the star formation in galaxies. Our results therefore highlight the need of additional high-J CO lines for better constraints of molecular gas properties and for better understanding of the baryon cycle of the galaxy ecosystem.

*Facilities:* CARMA, CAO:3.5m

*Software:* Miriad (Sault et al. 1995), Pipe3D (Sánchez et al. 2016b), IDL, matplotlib, astropy (Astropy Collaboration et al. 2013)

Y.C. and T.W. acknowledge support from the NSF through grants AST-1616199. R.C.L. acknowledges partial support by a NSF Astronomy and Astrophysics Postdoctoral Fellowship under award AST-2102625. J.B-B acknowledges support from the grant IA- 101522 (DGAPA-PAPIIT, UNAM) and funding from the CONACYT grant CF19-39578. DC acknowledges support by the Deutsche Forschungsgemeinschaft, DFG project number SFB956A. V. V. acknowledges support from the scholarship ANID-FULBRIGHT BIO 2016 - 56160020 and funding from NRAO Student Observing Support (SOS) - SOSPA7-014. V. V., acknowledge partial support from NSF-AST2108140.

This study makes use of data from the EDGE (<http://www.astro.umd.edu/EDGE/>) and CALIFA (<http://califa.caha.es/>) surveys and numerical values from the HyperLeda database (<http://leda.univ-lyon1.fr>). Support for CARMA construction was derived from the Gordon and Betty Moore Foundation, the Kenneth T. and Eileen L. Norris Foundation, the James S. McDonnell Foundation, the Associates of the California Institute of Technology, the University of Chicago, the states of California, Illinois, and Maryland, and the NSF. CARMA development and operations were supported by the NSF under a cooperative agreement and by the CARMA partner universities. This research is based on observations collected at the Centro Astronómico Hispano-Alemán (CAHA) at Calar Alto, operated jointly by the Max-Planck Institut für Astronomie (MPIA) and the Instituto de Astrofísica de Andalucía (CSIC). This research has made use of the NASA/IPAC Extragalactic Database (NED) which is operated by the California Institute of Technology, under contract with the National Aeronautics and Space Administration.

## REFERENCES

- Aalto, S., Beswick, R., & Jütte, E. 2010, *A&A*, 522, A59, doi: [10.1051/0004-6361/200913511](https://doi.org/10.1051/0004-6361/200913511)
- Aalto, S., Booth, R. S., Black, J. H., & Johansson, L. E. B. 1995, *A&A*, 300, 369
- Aalto, S., Johansson, L. E. B., Booth, R. S., & Black, J. H. 1991, *A&A*, 249, 323



- Astropy Collaboration, Robitaille, T. P., Tollerud, E. J., et al. 2013, *A&A*, 558, A33, doi: [10.1051/0004-6361/201322068](https://doi.org/10.1051/0004-6361/201322068)
- Bally, J., & Langer, W. D. 1982, *ApJ*, 255, 143, doi: [10.1086/159812](https://doi.org/10.1086/159812)
- Barrera-Ballesteros, J. K., García-Lorenzo, B., Falcón-Barroso, J., et al. 2015a, *A&A*, 582, A21, doi: [10.1051/0004-6361/201424935](https://doi.org/10.1051/0004-6361/201424935)
- Barrera-Ballesteros, J. K., Sánchez, S. F., García-Lorenzo, B., et al. 2015b, *A&A*, 579, A45, doi: [10.1051/0004-6361/201425397](https://doi.org/10.1051/0004-6361/201425397)
- Bolatto, A. D., Wong, T., Utomo, D., et al. 2017, *ApJ*, 846, 159, doi: [10.3847/1538-4357/aa86aa](https://doi.org/10.3847/1538-4357/aa86aa)
- Brown, T., & Wilson, C. D. 2019, *ApJ*, 879, 17, doi: [10.3847/1538-4357/ab2246](https://doi.org/10.3847/1538-4357/ab2246)
- Cao, Y., Wong, T., Xue, R., et al. 2017, *ApJ*, 847, 33, doi: [10.3847/1538-4357/aa88c5](https://doi.org/10.3847/1538-4357/aa88c5)
- Cardelli, J. A., Clayton, G. C., & Mathis, J. S. 1989, *ApJ*, 345, 245, doi: [10.1086/167900](https://doi.org/10.1086/167900)
- Casoli, F., Dupraz, C., & Combes, F. 1992, *A&A*, 264, 55
- Casoli, F., Dupraz, C., Combes, F., & Kazes, I. 1991, *A&A*, 251, 1
- Catalán-Torrecilla, C., Gil de Paz, A., Castillo-Morales, A., et al. 2015, *A&A*, 584, A87, doi: [10.1051/0004-6361/201526023](https://doi.org/10.1051/0004-6361/201526023)
- Chabrier, G. 2003, *PASP*, 115, 763, doi: [10.1086/376392](https://doi.org/10.1086/376392)
- Cid Fernandes, R., Stasińska, G., Mateus, A., & Vale Asari, N. 2011, *MNRAS*, 413, 1687, doi: [10.1111/j.1365-2966.2011.18244.x](https://doi.org/10.1111/j.1365-2966.2011.18244.x)
- Colzi, L., Sipilä, O., Roueff, E., Caselli, P., & Fontani, F. 2020, *A&A*, 640, A51, doi: [10.1051/0004-6361/202038251](https://doi.org/10.1051/0004-6361/202038251)
- Cormier, D., Bigiel, F., Jiménez-Donaire, M. J., et al. 2018, *MNRAS*, 475, 3909, doi: [10.1093/mnras/sty059](https://doi.org/10.1093/mnras/sty059)
- Crocker, A., Krips, M., Bureau, M., et al. 2012, *MNRAS*, 421, 1298, doi: [10.1111/j.1365-2966.2011.20393.x](https://doi.org/10.1111/j.1365-2966.2011.20393.x)
- Danielson, A. L. R., Swinbank, A. M., Smail, I., et al. 2013, *MNRAS*, 436, 2793, doi: [10.1093/mnras/stt1775](https://doi.org/10.1093/mnras/stt1775)
- Davis, T. A. 2014, *MNRAS*, 445, 2378, doi: [10.1093/mnras/stu1850](https://doi.org/10.1093/mnras/stu1850)
- den Brok, J. S., Bigiel, F., Chastenet, J., et al. 2023, arXiv e-prints, arXiv:2302.03044, doi: [10.48550/arXiv.2302.03044](https://doi.org/10.48550/arXiv.2302.03044)
- Di Teodoro, E. M., & Fraternali, F. 2015, *MNRAS*, 451, 3021, doi: [10.1093/mnras/stv1213](https://doi.org/10.1093/mnras/stv1213)
- Gallagher, M. J., Leroy, A. K., Bigiel, F., et al. 2018, *ApJ*, 858, 90, doi: [10.3847/1538-4357/aabad8](https://doi.org/10.3847/1538-4357/aabad8)
- Goldsmith, P. F., Heyer, M., Narayanan, G., et al. 2008, *ApJ*, 680, 428, doi: [10.1086/587166](https://doi.org/10.1086/587166)
- Henkel, C., & Mauersberger, R. 1993, *A&A*, 274, 730
- Henkel, C., Asiri, H., Ao, Y., et al. 2014, *A&A*, 565, A3, doi: [10.1051/0004-6361/201322962](https://doi.org/10.1051/0004-6361/201322962)
- Herrero-Illana, R., Privon, G. C., Evans, A. S., et al. 2019, *A&A*, 628, A71, doi: [10.1051/0004-6361/201834088](https://doi.org/10.1051/0004-6361/201834088)
- Hirota, A., Kuno, N., Sato, N., et al. 2010, *PASJ*, 62, 1261, doi: [10.1093/pasj/62.5.1261](https://doi.org/10.1093/pasj/62.5.1261)
- Jiménez-Donaire, M. J., Cormier, D., Bigiel, F., et al. 2017, *ApJL*, 836, L29, doi: [10.3847/2041-8213/836/2/L29](https://doi.org/10.3847/2041-8213/836/2/L29)
- Kewley, L. J., Dopita, M. A., Sutherland, R. S., Heisler, C. A., & Trevena, J. 2001, *ApJ*, 556, 121, doi: [10.1086/321545](https://doi.org/10.1086/321545)
- Kewley, L. J., Heisler, C. A., Dopita, M. A., et al. 2000, *ApJ*, 530, 704, doi: [10.1086/308397](https://doi.org/10.1086/308397)
- Kroupa, P. 2001, *MNRAS*, 322, 231, doi: [10.1046/j.1365-8711.2001.04022.x](https://doi.org/10.1046/j.1365-8711.2001.04022.x)
- Leroy, A. K., Usero, A., Schrubba, A., et al. 2017, *ApJ*, 835, 217, doi: [10.3847/1538-4357/835/2/217](https://doi.org/10.3847/1538-4357/835/2/217)
- Levy, R. C., Bolatto, A. D., Teuben, P., et al. 2018, *ApJ*, 860, 92, doi: [10.3847/1538-4357/aac2e5](https://doi.org/10.3847/1538-4357/aac2e5)
- Marino, R. A., Rosales-Ortega, F. F., Sánchez, S. F., et al. 2013, *A&A*, 559, A114, doi: [10.1051/0004-6361/201321956](https://doi.org/10.1051/0004-6361/201321956)
- Meier, D. S., & Turner, J. L. 2004, *AJ*, 127, 2069, doi: [10.1086/382904](https://doi.org/10.1086/382904)
- Milam, S. N., Savage, C., Brewster, M. A., Ziurys, L. M., & Wyckoff, S. 2005, *ApJ*, 634, 1126, doi: [10.1086/497123](https://doi.org/10.1086/497123)
- Morokuma-Matsui, K., Sorai, K., Sato, Y., et al. 2020, *PASJ*, 72, 90, doi: [10.1093/pasj/psaa084](https://doi.org/10.1093/pasj/psaa084)
- NASA/IPAC Extragalactic Database (NED). 2019, NASA/IPAC Extragalactic Database (NED), IPAC, doi: [10.26132/NED1](https://doi.org/10.26132/NED1)
- Paglione, T. A. D., Wall, W. F., Young, J. S., et al. 2001, *ApJS*, 135, 183, doi: [10.1086/321785](https://doi.org/10.1086/321785)
- Pety, J., Schinnerer, E., Leroy, A. K., et al. 2013, *ApJ*, 779, 43, doi: [10.1088/0004-637X/779/1/43](https://doi.org/10.1088/0004-637X/779/1/43)
- Puschnig, J. 2020, Dense Gas Toolbox, v1.2, Zenodo, doi: [10.5281/zenodo.3686329](https://doi.org/10.5281/zenodo.3686329)
- Rahman, N., Bolatto, A. D., Wong, T., et al. 2011, *ApJ*, 730, 72, doi: [10.1088/0004-637X/730/2/72](https://doi.org/10.1088/0004-637X/730/2/72)
- Rahman, N., Bolatto, A. D., Xue, R., et al. 2012, *ApJ*, 745, 183, doi: [10.1088/0004-637X/745/2/183](https://doi.org/10.1088/0004-637X/745/2/183)
- Rickard, L. J., & Blitz, L. 1985, *ApJL*, 292, L57, doi: [10.1086/184472](https://doi.org/10.1086/184472)
- Roman-Duval, J., Heyer, M., Brunt, C. M., et al. 2016, *ApJ*, 818, 144, doi: [10.3847/0004-637X/818/2/144](https://doi.org/10.3847/0004-637X/818/2/144)
- Romano, D., Matteucci, F., Zhang, Z.-Y., Papadopoulos, P. P., & Ivison, R. J. 2017, *MNRAS*, 470, 401, doi: [10.1093/mnras/stx1197](https://doi.org/10.1093/mnras/stx1197)
- Rosa-González, D., Terlevich, E., & Terlevich, R. 2002, *MNRAS*, 332, 283, doi: [10.1046/j.1365-8711.2002.05285.x](https://doi.org/10.1046/j.1365-8711.2002.05285.x)

- Rosolowsky, E., & Blitz, L. 2005, *ApJ*, 623, 826, doi: [10.1086/428897](https://doi.org/10.1086/428897)
- Sage, L. J., & Isbell, D. W. 1991, *A&A*, 247, 320
- Sánchez, S. F., Kennicutt, R. C., Gil de Paz, A., et al. 2012, *A&A*, 538, A8, doi: [10.1051/0004-6361/201117353](https://doi.org/10.1051/0004-6361/201117353)
- Sánchez, S. F., García-Benito, R., Zibetti, S., et al. 2016a, *A&A*, 594, A36, doi: [10.1051/0004-6361/201628661](https://doi.org/10.1051/0004-6361/201628661)
- Sánchez, S. F., Pérez, E., Sánchez-Blázquez, P., et al. 2016b, *RMxAA*, 52, 21. <https://arxiv.org/abs/1509.08552>
- Sánchez, S. F., Avila-Reese, V., Hernandez-Toledo, H., et al. 2018, *RMxAA*, 54, 217. <https://arxiv.org/abs/1709.05438>
- Sánchez-Menguiano, L., Sánchez, S. F., Pérez, I., et al. 2016, *A&A*, 587, A70, doi: [10.1051/0004-6361/201527450](https://doi.org/10.1051/0004-6361/201527450)
- Sault, R. J., Teuben, P. J., & Wright, M. C. H. 1995, in *Astronomical Society of the Pacific Conference Series*, Vol. 77, *Astronomical Data Analysis Software and Systems IV*, ed. R. A. Shaw, H. E. Payne, & J. J. E. Hayes, 433. <https://arxiv.org/abs/astro-ph/0612759>
- Sliwa, K., Wilson, C. D., Matsushita, S., et al. 2017, *ApJ*, 840, 8, doi: [10.3847/1538-4357/aa689b](https://doi.org/10.3847/1538-4357/aa689b)
- Tang, X. D., Henkel, C., Menten, K. M., et al. 2019, *A&A*, 629, A6, doi: [10.1051/0004-6361/201935603](https://doi.org/10.1051/0004-6361/201935603)
- Taniguchi, Y., & Ohya, Y. 1998, *ApJL*, 507, L121, doi: [10.1086/311696](https://doi.org/10.1086/311696)
- Topal, S. 2020, *MNRAS*, 495, 2682, doi: [10.1093/mnras/staa1146](https://doi.org/10.1093/mnras/staa1146)
- Vila-Vilaro, B., Cepa, J., & Zabludoff, A. 2015, *ApJS*, 218, 28, doi: [10.1088/0067-0049/218/2/28](https://doi.org/10.1088/0067-0049/218/2/28)
- Viti, S., Fontani, F., & Jiménez-Serra, I. 2020, *MNRAS*, 497, 4333, doi: [10.1093/mnras/staa2215](https://doi.org/10.1093/mnras/staa2215)
- Watson, W. D., Anicich, V. G., & Huntress, Jr., W. T. 1976, *ApJL*, 205, L165, doi: [10.1086/182115](https://doi.org/10.1086/182115)
- Wilson, T. L., & Rood, R. 1994, *ARA&A*, 32, 191, doi: [10.1146/annurev.aa.32.090194.001203](https://doi.org/10.1146/annurev.aa.32.090194.001203)
- Wong, T., Xue, R., Bolatto, A. D., et al. 2013, *ApJL*, 777, L4, doi: [10.1088/2041-8205/777/1/L4](https://doi.org/10.1088/2041-8205/777/1/L4)
- Young, J. S., & Sanders, D. B. 1986a, *ApJ*, 302, 680, doi: [10.1086/164029](https://doi.org/10.1086/164029)
- . 1986b, *ApJ*, 302, 680, doi: [10.1086/164029](https://doi.org/10.1086/164029)
- Young, J. S., & Scoville, N. Z. 1984, *ApJ*, 287, 153, doi: [10.1086/162673](https://doi.org/10.1086/162673)
- Zhang, Z.-Y., Romano, D., Ivison, R. J., Papadopoulos, P. P., & Matteucci, F. 2018, *Nature*, 558, 260, doi: [10.1038/s41586-018-0196-x](https://doi.org/10.1038/s41586-018-0196-x)

## APPENDIX

## A. ADDITIONAL GLOBAL PROPERTIES

The main galaxy parameters in the EDGE-CALIFA survey are summarized in the Tables 1-3 in Bolatto et al. (2017). In this appendix, we provide the additional global properties used in this study in Table 5.

**Table 5.** Galaxy Parameters in the EDGE-CALIFA Survey

Galaxy	$F_{12}$	$A_v$	$r_{\text{mol}}/r_e$	Median( $\Delta V$ )	sSFR	Incl	PA	$\theta$
	(Jy km/s)	(mag)		(km/s)	( $\text{Gyr}^{-1}$ )	( $^\circ$ )	( $^\circ$ )	(kpc)
(1)	(2)	(3)	(4)	(5)	(6)	(7)	(8)	(9)
ARP220	$447.4 \pm 3.1$	5.3	0.1	67.6	-0.5	57	13	2.6
IC0480	$78.8 \pm 2.5$	1.3	0.2	17.8	-1.3	90	-12	2.2
IC0540	$21.0 \pm 2.1$	1.7	...	...	-2.0	90	-11	1.0
IC0944	$91.1 \pm 3.3$	2.0	0.5	...	-2.0	68	21	3.4
IC1199	$44.9 \pm 2.5$	1.0	0.2	5.6	-1.7	75	-17	2.3
IC1683	$90.5 \pm 2.5$	2.0	0.1	8.7	-1.3	69	-13	2.4
IC2247	$70.3 \pm 2.4$	1.6	0.2	23.8	-1.5	90	39	2.1
IC2487	$53.7 \pm 2.7$	1.1	0.3	12.3	-1.5	90	-17	2.1
IC4566	$52.5 \pm 2.7$	1.4	0.4	8.1	-1.9	52	-14	2.7
IC5376	$8.4 \pm 1.2$	1.2	...	...	-1.8	90	4	2.5
NGC0447	$34.8 \pm 1.8$	0.6	...	10.3	-2.5	15	31	2.7
NGC0477	$35.8 \pm 2.6$	0.9	0.5	7.4	-1.4	73	-16	2.9
NGC0496	$41.5 \pm 1.9$	1.0	0.2	5.3	-1.2	72	40	3.0
NGC0523	$101.2 \pm 3.4$	1.4	0.5	10.7	-1.3	80	-4	2.3
NGC0551	$40.2 \pm 2.3$	0.8	0.3	8.0	-1.6	70	-35	2.5
NGC1167	$16.4 \pm 1.9$	2.0	...	6.6	-2.0	49	-16	2.4
NGC2253	$165.0 \pm 3.9$	1.1	0.2	4.6	-1.3	43	16	1.7
NGC2347	$83.8 \pm 2.7$	0.7	0.2	8.1	-1.4	45	5	2.2
NGC2410	$86.0 \pm 3.3$	1.6	0.4	10.5	-1.4	81	26	2.3
NGC2480	$13.1 \pm 1.4$	1.0	...	8.7	-1.0	90	-22	1.1
NGC2487	$54.5 \pm 3.4$	0.8	...	8.5	-1.8	38	12	2.4
NGC2623	$121.9 \pm 1.7$	3.6	...	29.6	-1.0	83	-13	2.7
NGC2639	$99.1 \pm 3.7$	2.1	0.2	9.7	-1.6	45	-42	1.5
NGC2730	$31.2 \pm 2.6$	0.5	...	7.2	-1.1	56	-38	1.9
NGC2906	$91.9 \pm 3.8$	0.8	...	7.7	-1.6	55	4	1.3
NGC2916	$29.4 \pm 2.5$	0.6	...	8.3	-1.4	51	6	1.8
NGC3303	$33.4 \pm 2.1$	1.4	0.2	10.3	-1.8	53	42	3.0
NGC3381	$15.5 \pm 2.0$	0.4	...	4.7	-1.1	26	-11	0.8
NGC3811	$92.2 \pm 3.5$	0.9	0.2	9.3	-1.3	43	34	1.5
NGC3815	$45.7 \pm 2.4$	0.8	0.2	8.7	-1.6	62	-19	1.8
NGC3994	$78.8 \pm 2.9$	1.0	0.1	9.9	-1.1	59	13	1.5
NGC4047	$196.6 \pm 3.9$	1.1	0.1	4.0	-1.3	42	-1	1.7
NGC4149	$78.8 \pm 2.5$	1.6	...	7.4	-1.9	83	-4	1.5
NGC4185	$13.0 \pm 1.9$	0.9	...	3.6	-1.7	49	-15	1.9
NGC4210	$49.2 \pm 2.8$	0.6	...	2.8	-1.6	46	-33	1.3
NGC4211N	$18.1 \pm 1.6$	2.1	...	...	-1.4	60	-35	3.3
NGC4470	$36.1 \pm 2.7$	0.5	...	4.4	-1.1	51	-2	1.1
NGC4644	$29.6 \pm 1.8$	1.1	0.4	4.9	-1.6	70	-39	2.4
NGC4676A	$77.3 \pm 2.6$	1.4	0.1	...	-1.5	64	-24	3.3
NGC4711	$40.9 \pm 2.5$	0.8	0.2	10.5	-1.5	59	43	2.0

**Table 5** *continued*

Table 5 (continued)

Galaxy	$F_{12}$	$A_v$	$r_{\text{mol}}/r_e$	Median( $\Delta V$ )	sSFR	Incl	PA	$\theta$
	(Jy km/s)	(mag)		(km/s)	( $\text{Gyr}^{-1}$ )	( $^\circ$ )	( $^\circ$ )	(kpc)
(1)	(2)	(3)	(4)	(5)	(6)	(7)	(8)	(9)
NGC4961	22.0 ± 2.0	0.4	...	8.5	-1.0	39	25	1.2
NGC5000	44.3 ± 2.1	1.3	...	3.9	-1.6	38	-3	2.7
NGC5016	67.8 ± 3.0	0.7	...	3.8	-1.4	45	-21	1.3
NGC5056	41.0 ± 2.2	0.4	0.3	6.8	-1.8	61	-12	2.7
NGC5205	23.9 ± 2.5	0.7	...	2.4	-1.7	56	20	0.9
NGC5218	416.9 ± 4.6	2.7	0.1	28.0	-1.5	51	4	1.4
NGC5394	168.6 ± 2.4	2.0	0.2	12.0	-1.0	71	1	1.7
NGC5406	62.6 ± 3.6	0.9	0.6	7.2	-1.7	46	-37	2.6
NGC5480	136.6 ± 4.2	1.0	...	10.9	-1.0	41	2	0.9
NGC5520	65.7 ± 2.9	0.8	...	2.1	-1.1	64	-26	0.9
NGC5614	228.0 ± 4.0	1.7	0.2	24.6	-2.0	36	-20	1.9
NGC5633	134.3 ± 3.6	1.0	...	10.0	-1.2	51	10	1.1
NGC5657	28.7 ± 2.1	1.3	...	10.1	-1.5	71	20	1.9
NGC5732	17.9 ± 1.9	0.6	...	...	-1.2	61	35	1.8
NGC5784	32.4 ± 1.9	...	0.2	8.6	...	28	-34	2.7
NGC5908	392.6 ± 4.5	2.1	0.3	60.9	-1.9	65	-28	1.6
NGC5930	136.4 ± 2.8	1.7	...	10.1	-1.2	71	-44	1.3
NGC5934	90.7 ± 2.5	2.1	0.2	32.3	-1.7	69	3	2.8
NGC5947	11.0 ± 1.3	0.5	0.2	5.9	-1.4	47	24	2.9
NGC5953	358.0 ± 4.4	1.7	...	12.8	-1.0	44	-39	1.0
NGC5980	137.7 ± 3.0	1.3	0.2	10.0	-1.3	76	11	2.0
NGC6004	66.8 ± 3.3	0.8	0.1	3.5	-1.6	39	10	1.9
NGC6060	132.7 ± 4.0	1.5	0.4	9.4	-1.5	59	11	2.1
NGC6155	81.1 ± 3.4	1.0	...	10.9	-1.1	51	-33	1.2
NGC6168	29.8 ± 2.4	1.1	0.1	9.8	-1.0	90	20	1.2
NGC6186	164.3 ± 3.9	1.6	0.2	11.4	-1.4	71	-18	1.4
NGC6301	59.2 ± 2.7	1.3	0.9	7.8	-1.4	57	-28	4.1
NGC6310	8.6 ± 1.3	0.9	...	...	-2.1	90	-20	1.6
NGC6314	33.2 ± 1.7	2.0	0.2	8.5	-2.3	66	-2	3.2
NGC6361	376.9 ± 3.8	2.6	0.3	48.3	-1.3	84	-36	1.9
NGC6394	38.1 ± 2.2	1.5	0.4	7.9	-1.6	73	30	4.2
NGC6478	144.1 ± 3.3	1.7	0.4	10.8	-1.5	77	34	3.3
NGC7738	98.9 ± 1.5	3.0	0.1	29.1	-1.2	64	42	3.3
NGC7819	32.1 ± 1.8	0.9	...	8.5	-1.1	60	14	2.4
UGC00809	6.0 ± 1.1	1.0	0.2	...	-1.1	83	22	2.0
UGC03253	14.3 ± 1.6	1.1	0.2	8.6	-1.7	61	30	2.0
UGC03539	56.1 ± 2.5	1.3	0.2	11.8	-1.2	90	20	1.6
UGC03969	46.4 ± 2.3	1.6	0.4	13.2	-1.5	80	44	4.0
UGC03973	33.1 ± 2.1	0.8	0.3	9.0	-1.1	37	26	3.3
UGC04029	56.6 ± 2.4	1.4	0.3	17.7	-1.8	90	-27	2.2
UGC04132	182.8 ± 3.6	1.7	0.3	32.5	-1.2	77	27	2.6
UGC04280	14.1 ± 1.5	0.9	...	8.2	-1.7	90	-3	1.7
UGC04461	32.3 ± 2.0	0.8	0.2	9.3	-1.1	78	-42	2.4
UGC05108	27.2 ± 1.6	2.0	0.3	8.5	-1.5	74	5	4.0
UGC05111	90.7 ± 2.5	2.2	0.5	35.2	-1.6	90	29	3.3
UGC05359	11.6 ± 1.2	1.0	0.5	2.9	-1.6	72	0	4.2
UGC05598	20.1 ± 1.8	1.1	0.2	10.3	-1.3	79	36	2.7
UGC07012	9.0 ± 1.3	0.4	...	6.6	-0.9	59	15	1.5
UGC08107	80.0 ± 2.4	1.5	0.3	52.1	-1.5	84	43	4.1
UGC08267	50.2 ± 2.2	2.2	0.3	12.9	-1.5	85	40	3.5
UGC09067	45.3 ± 2.4	1.0	0.3	7.7	-1.3	69	14	3.9

Table 5 continued

Table 5 (continued)

Galaxy	$F_{12}$	$A_v$	$r_{\text{mol}}/r_e$	Median( $\Delta V$ )	sSFR	Incl	PA	$\theta$
	(Jy km/s)	(mag)		(km/s)	( $\text{Gyr}^{-1}$ )	( $^\circ$ )	( $^\circ$ )	(kpc)
(1)	(2)	(3)	(4)	(5)	(6)	(7)	(8)	(9)
UGC09476	$47.2 \pm 3.1$	0.7	0.2	...	-1.3	53	2	1.6
UGC09537	$38.7 \pm 2.3$	1.4	0.6	10.1	-1.7	90	-43	4.4
UGC09542	$28.9 \pm 2.0$	1.2	0.3	11.1	-1.4	76	31	2.7
UGC09665	$61.6 \pm 2.8$	1.2	0.2	29.0	-1.3	90	-35	1.2
UGC09759	$46.0 \pm 2.2$	1.6	...	9.7	-1.7	63	-43	1.7
UGC09873	$10.4 \pm 1.2$	1.3	0.2	9.3	-1.2	83	36	3.1
UGC09892	$18.0 \pm 1.6$	1.0	0.3	8.7	-1.5	90	13	2.8
UGC09919	$5.8 \pm 1.1$	1.0	...	...	-1.3	90	-10	1.6
UGC10043	$66.0 \pm 2.9$	1.3	...	10.2	-1.6	90	-29	1.1
UGC10123	$97.4 \pm 2.9$	1.7	0.2	27.6	-1.5	90	-37	1.8
UGC10205	$37.4 \pm 2.2$	2.0	0.2	10.1	-1.9	59	36	3.2
UGC10380	$17.0 \pm 1.7$	1.7	0.2	8.9	-1.7	90	-29	3.8
UGC10384	$69.1 \pm 2.2$	1.5	0.2	13.5	-1.0	90	23	2.4
UGC10710	$36.2 \pm 2.2$	1.3	0.4	7.5	-1.8	84	-36	4.1

NOTE— (1) Galaxy name; (2)  $^{12}\text{CO}$  integrated flux or its upper limit; (3) Nebular extinction from Pipe3D; (4) Median velocity dispersion; (5) Specific star formation from Pipe3D; (6) Morphology inclination from HyperLEDA; (7) Morphology position angle from CALIFA; (8) Linear resolution of the CO mapping.

## B. THE PEAK SIGNAL-TO-NOISE MAP OF $^{13}\text{CO}$

Figure 8 show the peak signal-to-noise (SNR) of  $^{13}\text{CO}$  in all of the channels without any masking. We obtain it by finding the highest peak  $^{13}\text{CO}$  temperature in the spectrum along each spatial pixel, and then dividing by the corresponding sensitivity. The regions we detect integrated  $^{13}\text{CO}$  (shown as black contours in Figure 8) enclose the high peak SNR pixels, which support the significance our detection.

## C. AZIMUTHALLY STACKED $\mathcal{R}_{12/13}^{\text{stack}}$ OF EACH GALAXY

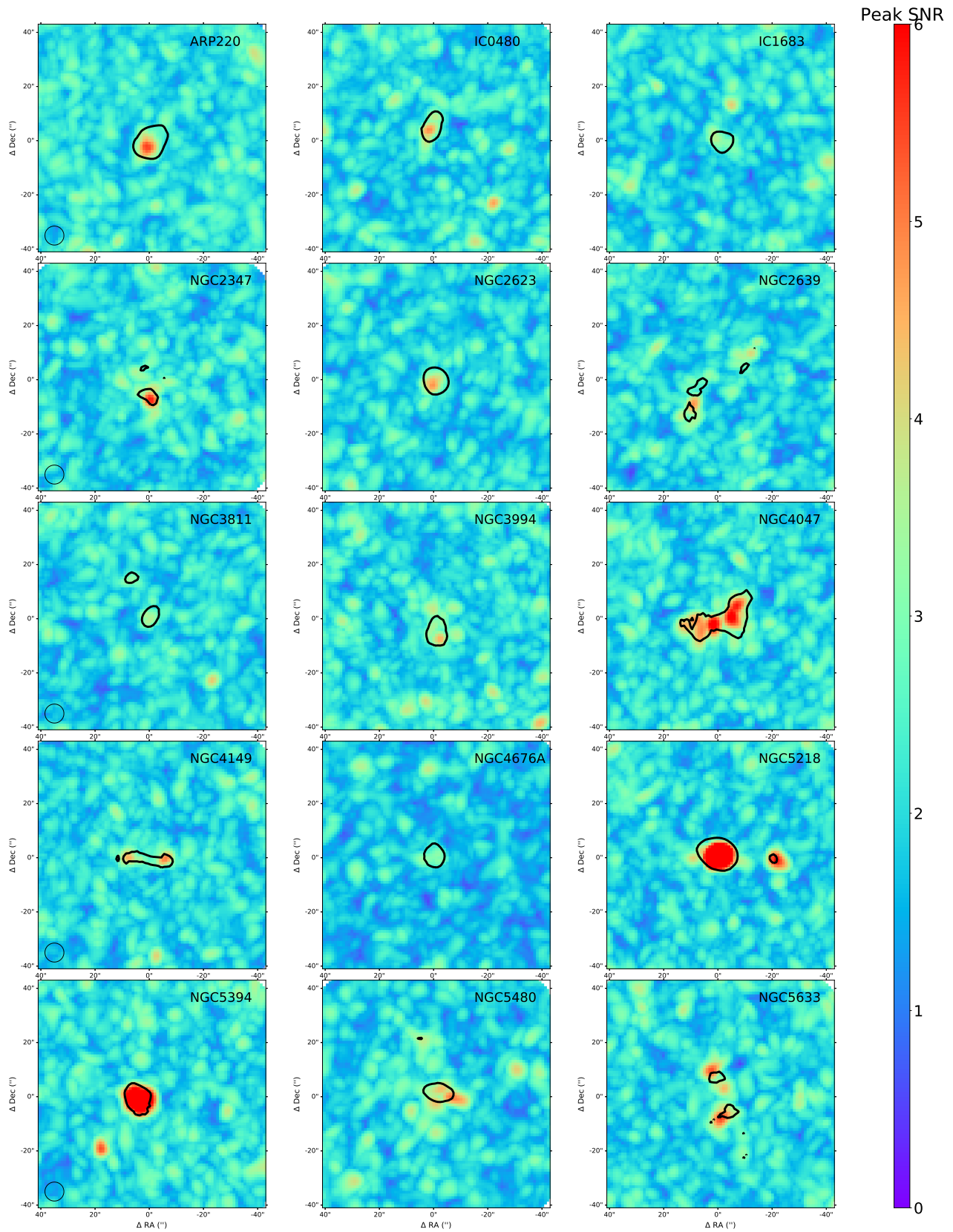
Figure 9 show two examples of the azimuthally stacked spectra from which we derive the  $\mathcal{R}_{12/13}^{\text{stack}}$ . For IC 0944, we detect the integrated intensity of the stacked  $^{13}\text{CO}$  ( $I_{13}^{\text{stack}}$ ) in the first three radii bins with  $S/N > 4$ . For NGC 2906,  $I_{13}^{\text{stack}}$  are detected in the first four bins with  $S/N > 4$ . In these bins, the stacked  $^{13}\text{CO}$  spectra peak in the shifted central velocity, and are well fitted by Gaussian profiles (shown as the blue shaded regions).

Figure 10 shows  $\mathcal{R}_{12/13}^{\text{stack}}$  profiles of each individual galaxy of our sample. We show the interacting galaxies with star symbols to distinguish them from the others. Across the sample, there are a wide variety of radial profiles. In each individual galaxy, the radial variations of  $\mathcal{R}_{12/13}^{\text{stack}}$  are within  $\sim 0.2$  dex in most cases. Any annulus with stacked  $^{13}\text{CO}$  below the detection limit of  $3\sigma$  is omitted. For the non-interacting galaxies, we show those with bars using cross symbols while the others are shown in filled circles.

## D. CORRELATIONS BETWEEN KPC-SCALE $\mathcal{R}_{12/13}$ AND RESOLVED PROPERTIES

Figure 11 shows the correlations between resolved  $\mathcal{R}_{12/13}$  and other local properties for all the  $I_{13}$  detections in the non-interacting galaxies in the EDGE-CALIFA survey. The Spearman's rank correlation coefficients  $r$  and the probabilities of no correlation  $P_0$  are listed in Table 6.

The strong apparent dependence on  $I_{12}$  is mainly due to the sensitivity bias toward lower values in our  $\mathcal{R}_{12/13}$  measurements when  $I_{12}$  is weak (panel (a)). In the lower  $I_{12}$  regime, only grids with strong  $I_{13}$  and lower  $\mathcal{R}_{12/13}$  are detected. Grids with  $\mathcal{R}_{12/13} < 5$  experience the most bias, and act to drive the strong positive correlation between  $\mathcal{R}_{12/13}$  and  $I_{12}$ . Since  $^{12}\text{CO}$  moment 2 (panel (c)) and nebular extinction  $A_v$  (panel (g)) increase with  $I_{12}$ , the apparent increasing trends of  $\mathcal{R}_{12/13}$  with them could also result from bias due to limited sensitivity at lower  $I_{12}$ .



**Figure 8.** The peak signal-to-noise map of  $^{13}\text{CO}$  for the 30 galaxies with resolved  $^{13}\text{CO}$  detected from the EDGE survey. The black contours overlaid show the  $^{13}\text{CO}$  intensity observed with  $\text{S/N} > 4$ .

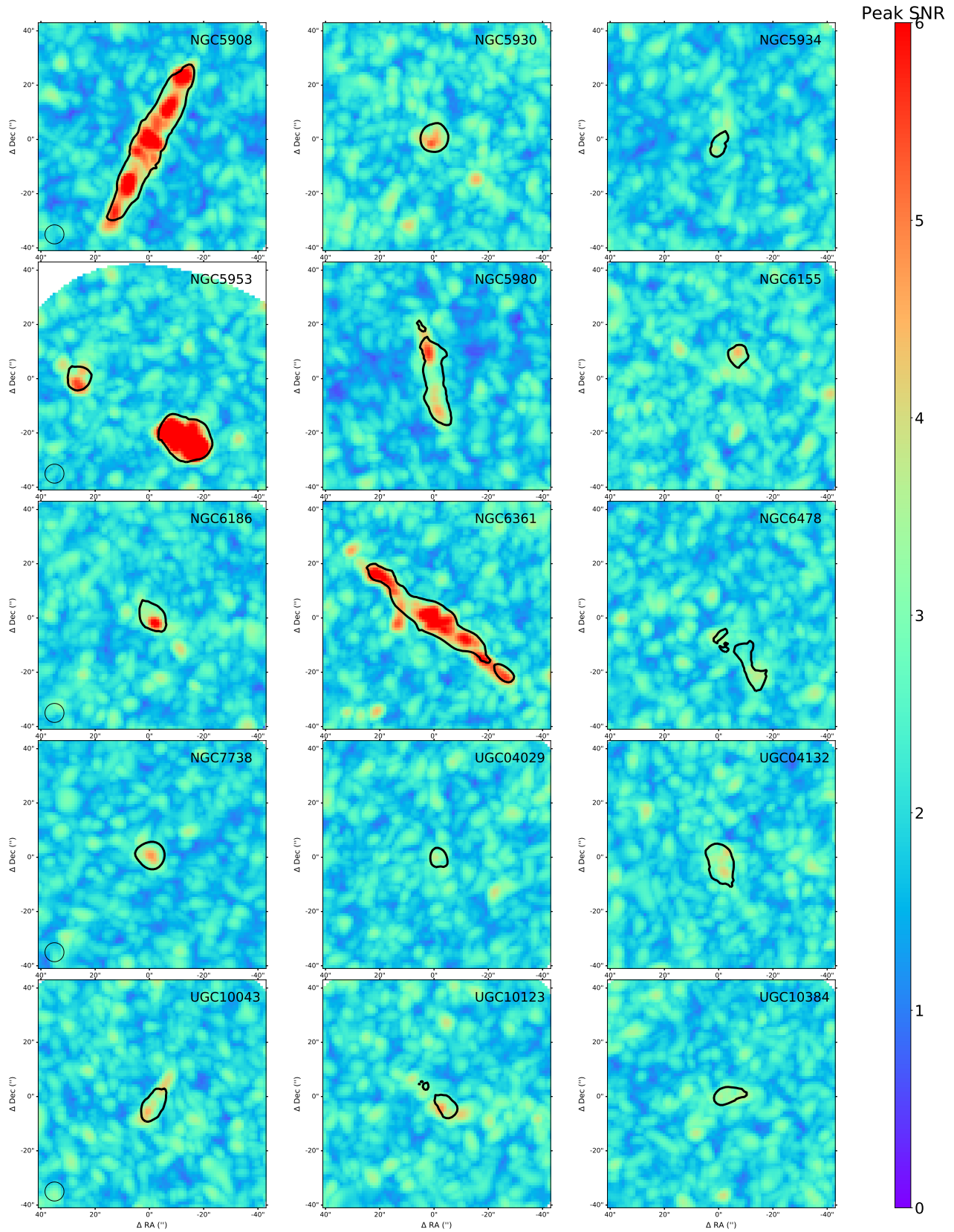
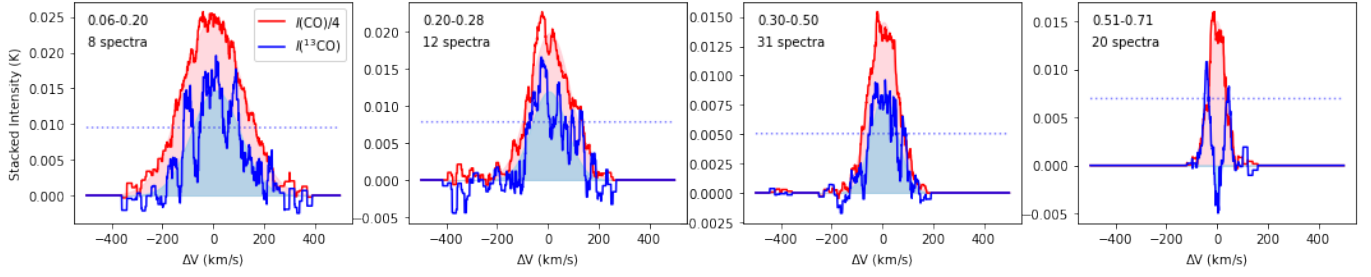
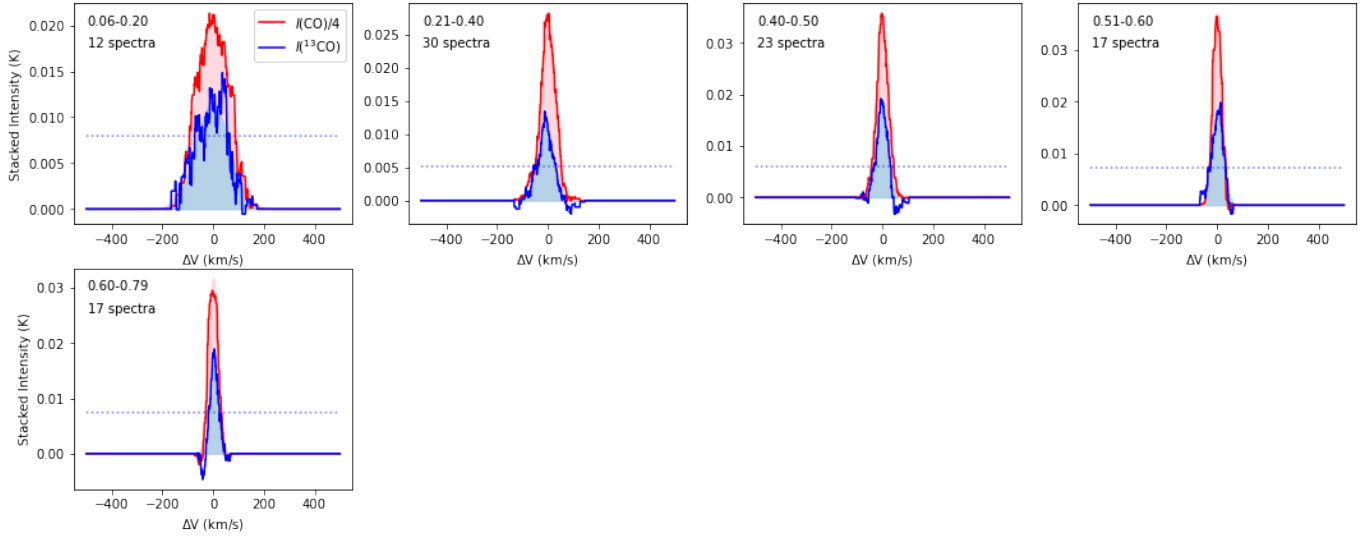


Figure 8. (Continued).

## IC0944



## NGC2906



**Figure 9.** Azimuthally stacked spectra of IC 0944 (*top*) and NGC 2906 (*bottom*). Each panel show the results of a radial bin adjusted following the method described in 3.3. In the top left corner of each panel, we show the radial bin ranges in units of  $r_{\text{gal}}/r_{25}$  and the numbers of the spectra used in the stacking. The blue lines are the  $^{13}\text{CO}$  spectra and the red lines are the  $^{12}\text{CO}$  spectra scaled down by a factor of 4. The blue vertical lines show the channel noise of the  $^{13}\text{CO}$  stacked spectrum derived following Equation 4. The red and blue shaded regions show the Gaussian fitted integrated fluxes of  $^{12}\text{CO}$  and  $^{13}\text{CO}$  used for the stacked line ratios.

Meanwhile, there is a tight correlation between  $\mathcal{R}_{12/13}$  and gas fraction shown in panel (k), which is not entirely due to detection bias, as the increasing trend is still obvious if we exclude grids with  $\mathcal{R}_{12/13} < 5$  from this panel. Similar to results based on  $\mathcal{R}_{12/13}^{\text{stack}}$ , this correlation may reflect the association of higher  $I_{13}$  with higher stellar surface density on kpc scales.



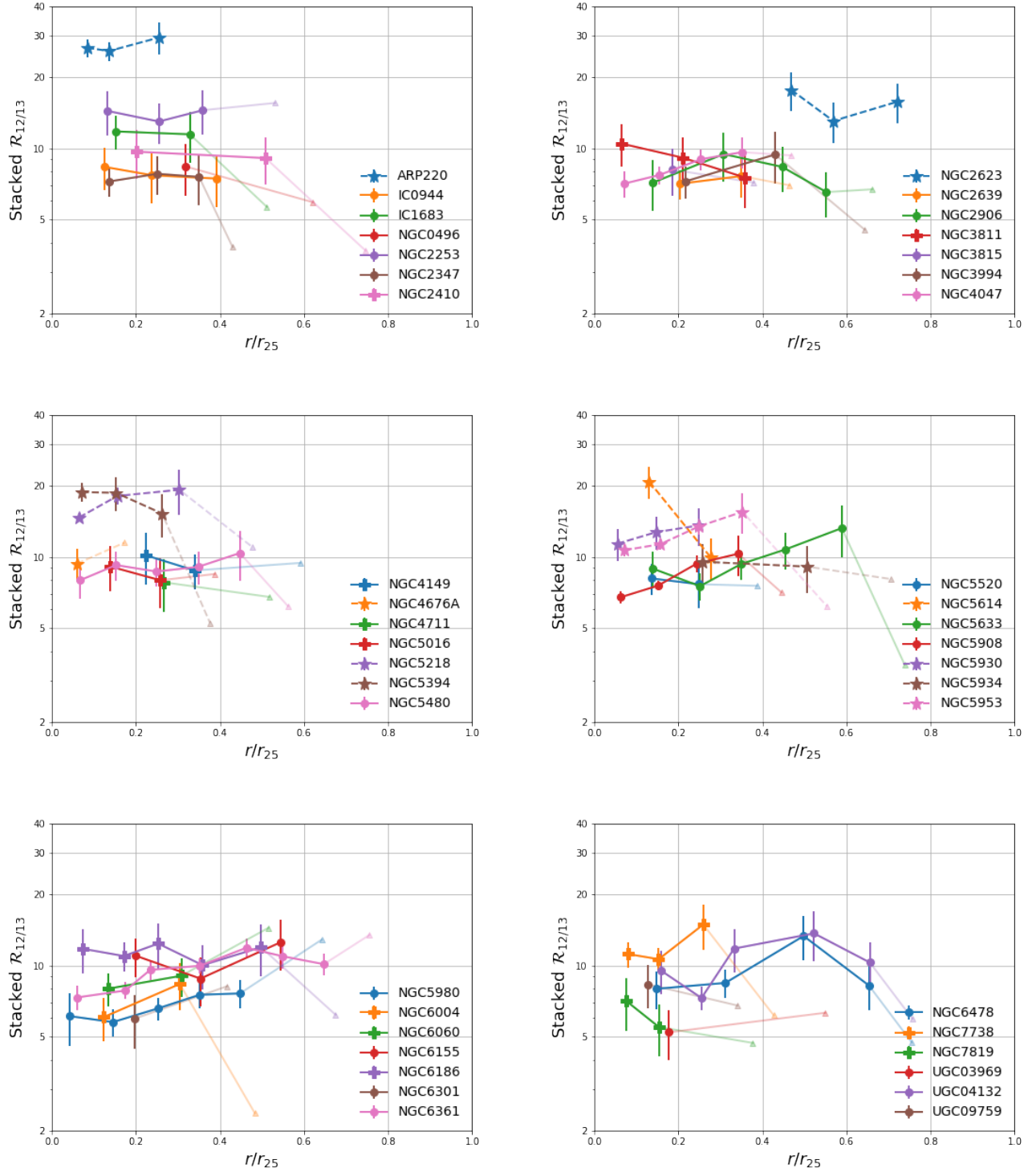


**Figure 10.** Radially averaged  $\mathcal{R}_{12/13}^{\text{stack}}$  profiles of the 41 galaxies with  $I_{13}^{\text{stack}}$  detected with  $S/N > 4$  in our sample. The galactocentric radius for each galaxy is normalized to its  $r_{25}$ . Spectra of  $^{13}\text{CO}$  and  $^{12}\text{CO}$  are shifted and stacked at each normalized radii bin to derive  $\mathcal{R}_{12/13}^{\text{stack}}$ . Interacting galaxies are highlighted with star symbols. Cross symbols show the non-interacting galaxies with bars, and filled circles show the other non-interacting galaxies. The lower limit of  $\mathcal{R}_{12/13}^{\text{stack}}$  in the bins with  $I_{13}^{\text{stack}}$  below the detection threshold of 4 are shown in triangles. We are able to detect stacked  $^{13}\text{CO}$  out to a radius of  $\sim 0.4r_{25}$  in most galaxies.

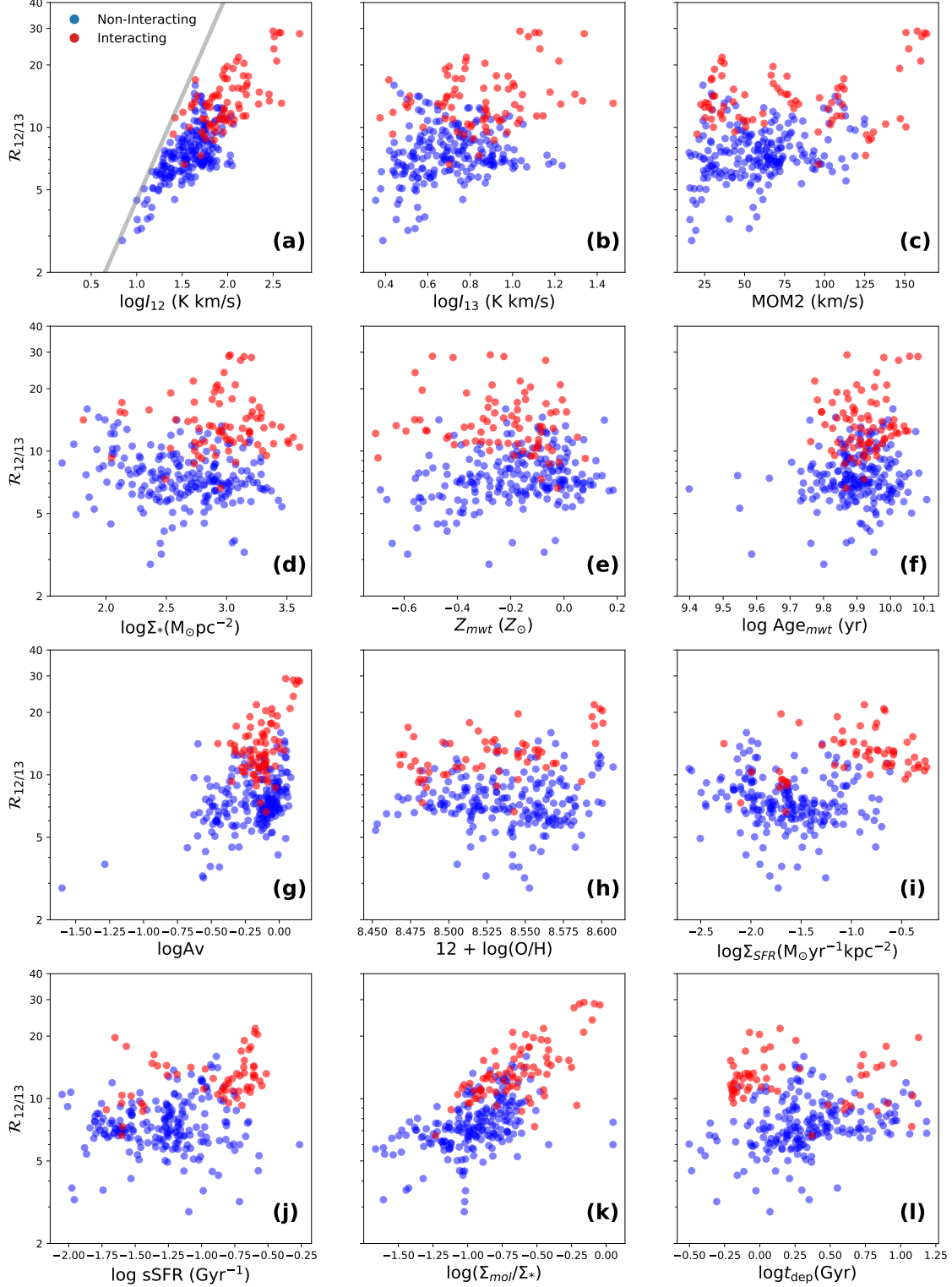


**Figure 11.** Resolved line ratio  $\mathcal{R}_{12/13}$  as functions local parameters for regions where  $I_{13}$  is detected with  $S/N > 4$ . The Spearman rank correlation test results are shown in Table 6. The gray line in panel (a) corresponds to the upper boundary of our  $\mathcal{R}_{12/13}$  measurements imposed by a constant  $I_{13}$  detection of the sample (corresponding to the horizontal gray line in panel (a) of Figure 3). In panels (h), (i), (j), (l), we exclude the grids which are identified as star forming regions with the BPT diagnostics. The filled circles show the individual  $\mathcal{R}_{12/13}$  measurements for non-interacting (blue) and interacting (red) galaxies.

**Table 6.** Spearman’s rank correlation coefficients between  $\mathcal{R}_{12/13}$  and local parameters

Parameter	Note	Ref	All galaxies		Non-interacting galaxies		Interacting galaxies	
			$r_s$	$P_0$	$r_s$	$P_0$	$r_s$	$P_0$
$I_{12}$	$^{12}\text{CO}$ intensity	1	0.74	< 0.001	0.62	< 0.001	0.62	< 0.001
$I_{13}$	$^{13}\text{CO}$ intensity	2	0.32	< 0.001	0.21	0.0022	0.20	0.079
MOM2	$^{12}\text{CO}$ Moment2	1	0.24	< 0.001	0.25	< 0.001	0.09	0.43
$\Sigma_*$	Stellar mass surface density	3	0.16	0.0069	-0.14	0.048	-0.02	0.87
$Z_{\text{mwt}}$	Mass weighted stellar metallicity	3	0.01	0.88	0.21	0.0024	-0.18	0.12
$\text{Age}_{\text{mwt}}$	Mass weighted stellar age	3	0.11	0.073	0.04	0.6	0.06	0.63
$A_v$	Nebular extinction from Pipe3D	3	0.26	< 0.001	0.33	< 0.001	0.35	0.002
$12 + \log(\text{O}/\text{H})$	Gas phase metallicity from O3N2	3	-0.03	0.65	-0.00	0.98	0.38	0.0027
$\Sigma_{\text{SFR}}$	Star formation rate surface density	3	0.24	< 0.001	-0.16	0.02	0.06	0.64
$s\text{SFR}$	Specific star formation rate	3	0.32	< 0.001	0.07	0.33	0.37	0.0036
$\Sigma_{\text{mol}}/\Sigma_*$	Molecular gas to stellar mass fraction	2	0.65	< 0.001	0.52	< 0.001	0.60	< 0.001
$t_{\text{dep}}$	Depletion time assuming constant $X_{12\text{CO}}$	2	0.04	0.56	0.31	< 0.001	0.07	0.57

NOTE— References: 1. Bolatto et al. (2017); 2. This work; 3. Sánchez et al. (2016b).